materials

MDPI

Review

Recent Progress in Low-Power-Consumption Metal Oxide Semiconductor Gas Sensors

Yu Zhang [1], Renbo Li [2,3], Ruqi Guo [2,3], Mingzhi Jiao [2,3,*], Gang Wang [2,3,*] and Zhikai Zhao [2,3,*]

[1] School of Safety Engineering, China University of Mining and Technology, Xuzhou 221116, China; zhangy74@cumt.edu.cn
[2] National & Local Joint Engineering Laboratory for Internet Application Technology in Mines, Xuzhou 221116, China; ts24060193p31@cumt.edu.cn (R.L.); ts24060009a31@cumt.edu.cn (R.G.)
[3] School of Information and Control Engineering, China University of Mining and Technology, Xuzhou 221116, China
* Correspondence: mingzhijiao@cumt.edu.cn (M.J.); wanggang@cumt.edu.cn (G.W.); zhaozhikai@cumt.edu.cn (Z.Z.)

Abstract

Metal oxide semiconductor (MOS) gas sensors offer several advantages, including low cost, high accuracy, and ease of miniaturization. Thus, they are excellent candidates for environmental monitoring and food spoilage detection applications, particularly in the safe Internet of Things field or for portable instruments. Typically, there are two general routes for realizing low-power-consumption MOS gas sensors: room-temperature MOS gas sensors or MEMS MOS gas sensors. The review focuses on the detection of four typical gases, namely methane, hydrogen, carbon monoxide, and nitrogen dioxide, systematically summarizing and analyzing the most recent results of low-power-consumption MOS gas sensors. The 2D materials, MOS composites, and 3D structured composites exhibit excellent room-temperature gas detection capabilities. The mechanism of the room-temperature gas sensors is also discussed in detail. Another route is MEMS MOS gas sensors. First, the progress of the micro-hotplate research is introduced. Then, several of the latest reported MEMS MOS gas sensors are shown and compared. The gas sensing mechanism of these MEMS MOS gas sensors is also given. The paper will provide a valuable guide for researchers in the MOS gas sensor field, particularly for those working towards low-power-consumption MOS gas sensors.

Keywords: MOS gas sensors; room temperature; MEMS; low power-consumption; methane; carbon monoxide; nitrogen dioxide; hydrogen

check for updates

Academic Editor: Marina N. Rumyantseva

Received: 15 September 2025
Revised: 14 October 2025
Accepted: 20 October 2025
Published: 24 October 2025

Citation: Zhang, Y.; Li, R.; Guo, R.; Jiao, M.; Wang, G.; Zhao, Z. Recent Progress in Low-Power-Consumption Metal Oxide Semiconductor Gas Sensors. *Materials* **2025**, *18*, 4864. https://doi.org/10.3390/ma18214864

Copyright: © 2025 by the authors. Licensee MDPI, Basel, Switzerland. This article is an open access article distributed under the terms and conditions of the Creative Commons Attribution (CC BY) license (https://creativecommons.org/licenses/by/4.0/).

1. Introduction

As the economy grows, more hazardous gases can be found in the outdoors or in factories. Methane can be found in coal mines or the kitchen. It can give rise to an explosion or severe combustion in the event of a leak. Furthermore, methane contributes much more to the greenhouse effect than carbon dioxide. Hydrogen is a promising fuel considering its high efficiency and cleanliness. However, it has a relatively wide explosion concentration range (from 4% to 75.6%). Additionally, nitrogen dioxide and carbon monoxide are two highly toxic gases that can cause severe harm to humans when humans are exposed to high concentrations for a short period. Thus, accurate monitoring of the above four gases is necessary to ensure city safety. Several gas sensor technologies, including optical, electrochemical, metal oxide semiconductor resistive, and catalytic combustion gas sensors, have

been utilized for gas safety monitoring. Metal oxide semiconductor (MOS) resistive gas sensors offer advantages such as low cost, ease of miniaturization, high accuracy, and a low detection limit, making them widely applicable in safety monitoring [1]. However, MOS gas sensors generally consume high power due to heater integration, casting a challenge for safe Internet of Things applications or portable devices. Low-power-consumption MOS gas sensors are gaining increasing attention, particularly in light of the power constraints in many applications. Core technologies for low-power-consumption gas sensors can be categorized into two main types: room-temperature solutions and MEMS-based designs [2–4]. Both approaches achieve energy efficiency through material innovation and structural-material optimization, respectively, accelerating the development of low-power-consumption gas sensors. The rest of the paper is organized in the following way: First, the progress of room-temperature gas sensors is introduced, with focus on the materials innovation and working mechanism discussion; Secondly, the recent development of MEMS gas sensors is described, with emphasis on micro-hotplate design and sensing materials; Thirdly, the challenge and prospects of low-power-consumption MOS gas sensors are discussed. Ultimately, the conclusion is presented regarding the current state of the art of the two solutions for low-power-consumption MOS gas sensors.

2. Room-Temperature Gas Sensors

Traditional metal oxide gas sensors require operation above room temperature, with heaters being the primary source of power consumption. These devices also pose safety risks due to the detection of flammable and explosive gases, as well as issues such as time-consuming preheating and significant material heat loss. In contrast, room-temperature gas sensors operate without heating, offering advantages such as no preheating required, low power consumption, minimal material heat loss, a simple structure, and reduced high-temperature hazards. These outstanding benefits have attracted considerable attention from researchers, who have conducted extensive studies on room-temperature gas sensors, with a particular focus on detectors for methane (CH_4), hydrogen (H_2), carbon monoxide (CO), and nitrogen dioxide (NO_2). NO_2 is a typical oxidative gas, while the other three gases are reductive. The four gases are chosen due to their wide existence in environmental and industrial scenarios.

2.1. Room-Temperature CO Sensors

Carbon monoxide is a rather lethal gas, causing severe death in a few minutes when the concentration is higher than 1200 ppm. A review by He et al. has summarized and compared many relevant works before 2024 [5]. Here, we will introduce some excellent work on room-temperature CO sensors published after 2024. Noble metal decoration can decrease the working temperature of metal oxide semiconductors. For example, Pd-CuO-$SnSe_2$ can respond to 200 ppm CO in 13 s [6]. It is reported that 1 wt% Pt-SnO_2 nanoceramics can react with 400 ppm CO at room temperature, yielding a response value of 2427 [7]. Wu et al. reported that 0.1Au-ZnO can respond to 100 ppm CO at room temperature in 61 s with a value of 139.75 [8]. The sensing mechanism of Au-ZnO can be explained in two aspects: the Schottky barrier and the catalytic function of Au. Since the work function of Au is lower than that of the conduction band of ZnO, electrons at the conduction band of ZnO will flow into the surface of Au and form Schottky barriers, enriching the number of electrons in Au and enlarging the surface depletion layer of ZnO. Schottky barriers will amplify resistance variations and inhibit electron-hole recombination, as shown in Figure 1a. Au with a higher electron density can enhance oxygen adsorption and dissociation, as shown in Figure 1b,c. Au will facilitate oxygen adsorption when the Au-ZnO is in the air. In CO, Au from the composite enhances the adsorption and dissociation of CO, thereby increasing the CO

surface reaction and sensing. CuO-SnO_2 nanotubes were synthesized by assembly on the carbon nanotube templates, followed by subsequent calcination [9]. The optimal sensor can respond to 300 ppm in 56 s. The response value can be as high as 1.34, with an ultra-low detection limit of 159 ppb. Xie et al. successfully synthesized SnO_2-NiO through the MOF template [10]. The sensor exhibits a response value of 5.48 toward 100 ppm CO in 56 s, with a detection limit as low as one ppm CO. The enhanced sensing performance of SnO_2-NiO can be attributed to the p-n heterojunction effect, as seen in Figure 1d. When the material is exposed to air, oxygen will trap electrons from the conduction band, increasing the number of hole carriers and forming a hole stacking layer, which will reduce the resistance of the sensor. When the sensor is exposed to CO, the trapped electrons recombine with the holes, causing the hole stacking layer to become thinner and the depletion layer to become thicker, which in turn increases the sensor resistance, as shown in Figure 1d.

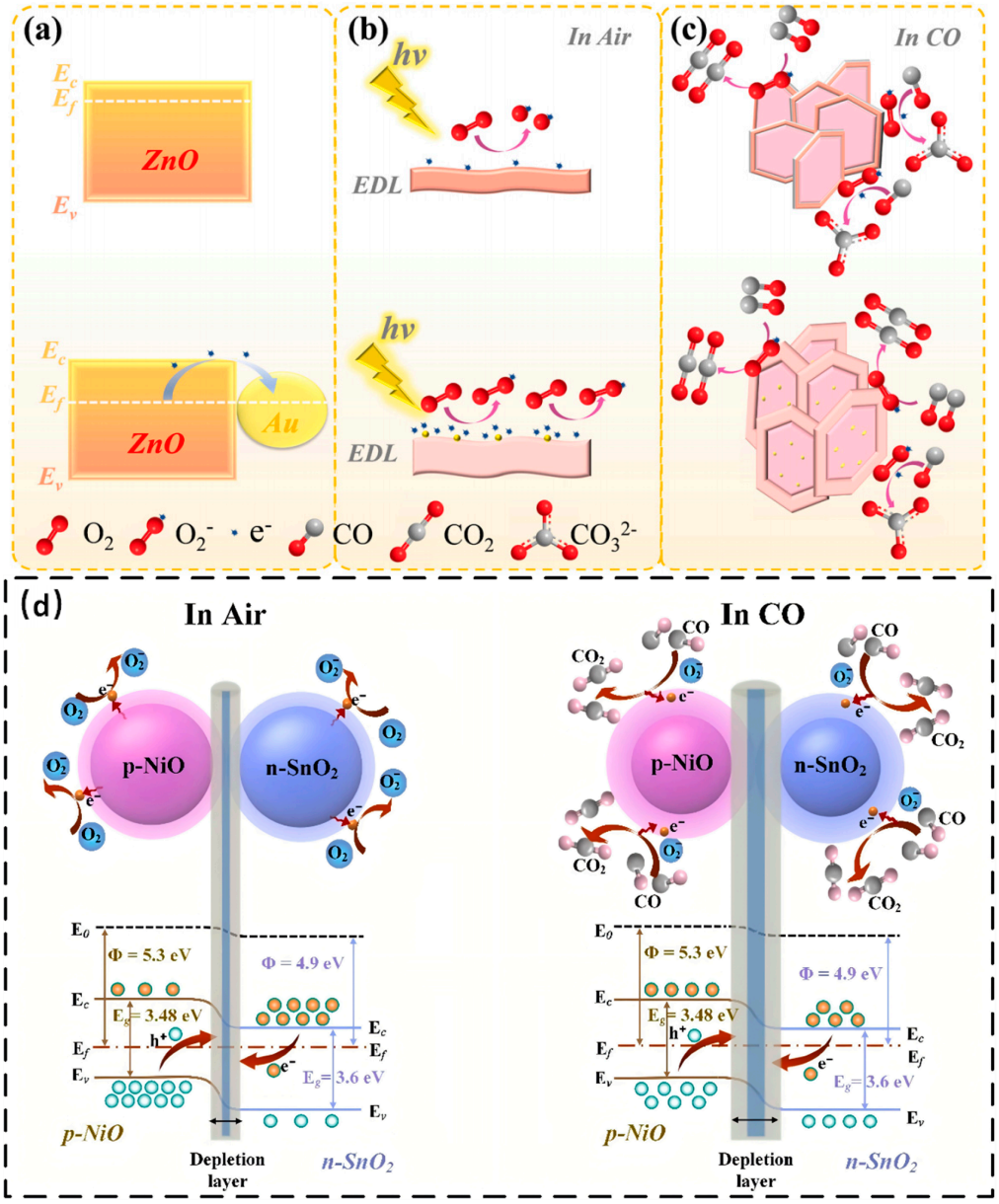


Figure 1. (**a**) The energy band structure of ZnO and Au-ZnO [8]; (**b**,**c**) The mechanism of Au nanoparticles on Au/ZnO and the reaction of CO on the surface of samples [8]; (**d**) diagram of CO-sensing mechanism from p-NiO/n-SnO_2 composites [10].

Furthermore, NiO-$Ti_3C_2T_x$ (MXene) composite was reported to respond to 400 ppm CO in only 8 s, with a response value of 1.3 [11]. The excellent sensing properties of NiO-$Ti_3C_2T_x$ are due to the superior characteristics of $Ti_3C_2T_x$. The outer surface of $Ti_3C_2T_x$ can be functionalized by different groups such as -F, -OH, or =O [12,13]. These groups can serve as attachment sites for surface-functional molecules, thereby enhancing the selectivity and sensitivity of the gas sensors. $Ti_3C_2T_x$ with -F and -OH groups have significantly different band gaps as well (0.72 eV for -F and 1.07 eV for -OH). In addition, $Ti_3C_2T_x$ has a room temperature conductivity of up to 10,000 S cm^{-1} [14,15].

As shown in Table 1, carbon-based composites exhibit good sensitivity and response speed to CO. For example, MWCNT/SnO_2 composites can react to 300 ppm CO in 5 s with a response value of 1.80 [16]. MWCNT and SnO_2 will form a p-n junction when the two come in contact, since MWCNT is a p-type material and SnO_2 is a typical n-type semiconductor. Furthermore, rGO-wrapped SnS_2 nanospheres can respond to 10 ppm CO in 11 s as well, with a response value as high as 10 [17]. On the one hand, a heterojunction between n-type SnS_2 and p-type rGO will enhance the CO response; on the other hand, the presence of numerous defect sites on the rGO surface will further increase the CO response.

Table 1. Comparison of the performance of various room-temperature CO-sensing materials.

Sensing Material	Conc. (ppm)	Response Value (R_g/R_a or R_a/R_g)	Response/Recovery Time (s)	Reference
Pd/CuO Nanorods/$SnSe_2$ Nanoflower	200	1.53	13/58	[6]
1 wt% Pt/SnO_2 nanoceramics	400	2427	-/-	[7]
0.10Au-decorated ZnO nanosheets	100	139.75	61/61	[8]
Au-Loaded WS_2/SnO_2	1	12.6	-/-	[18]
MOF-derived SnO_2/NiO	50	5.48	56/4	[9]
CuO/SnO_2 Hollow-Sphere	300	1.40	-/-	[5]
NiO/$Ti_3C_2T_x$	400	1.43	8/16	[11]
PANI/Ti_3AlC_2/CeO_2	500	1.17	347/-	[19]
MWCNTs/SnO_2	300	1.80	5/7	[16]
rGO wrapped SnS_2 nanosphere	10	10	11/10	[17]

2.2. Room-Temperature NO_2 Sensor

Recently, 2D materials such as reduced graphene oxide composites, Mxene, and transition metal dichalcogenides have been reported to detect NO_2 with excellent performance, even at room temperature. For example, rGO/CuO nanoflakes can respond to 5 ppm NO_2 at room temperature in only 6.8 s, with a response value of 1.26 [20]. rGO/In_2O_3 was found to have an ultrahigh response value of 1177 toward one ppm NO_2 [21]. In_2O_3/Ti_3C_2 nanosheets can respond to 100 ppm NO_2 in 18 s, with a response value of 371.19 [22]. The mechanism for room-temperature NO_2 sensing from In_2O_3/Ti_3C_2 is attributed to the Schottky barrier, as shown in Figure 2.

A detailed comparison of the room-temperature NO_2 sensing performance of 2D materials, as recently reported, is presented in Table 2. Even though In_2O_3/Ti_3C_2 nanosheets can respond to 100 ppm NO_2 in 18 s, the recovery time is as long as 95 s. The prolonged recovery time of the materials is attributed to intense interactions between NO_2 and the In_2O_3/Ti_3C_2 nanosheets, which pose challenges for the desorption of NO_2 gas.

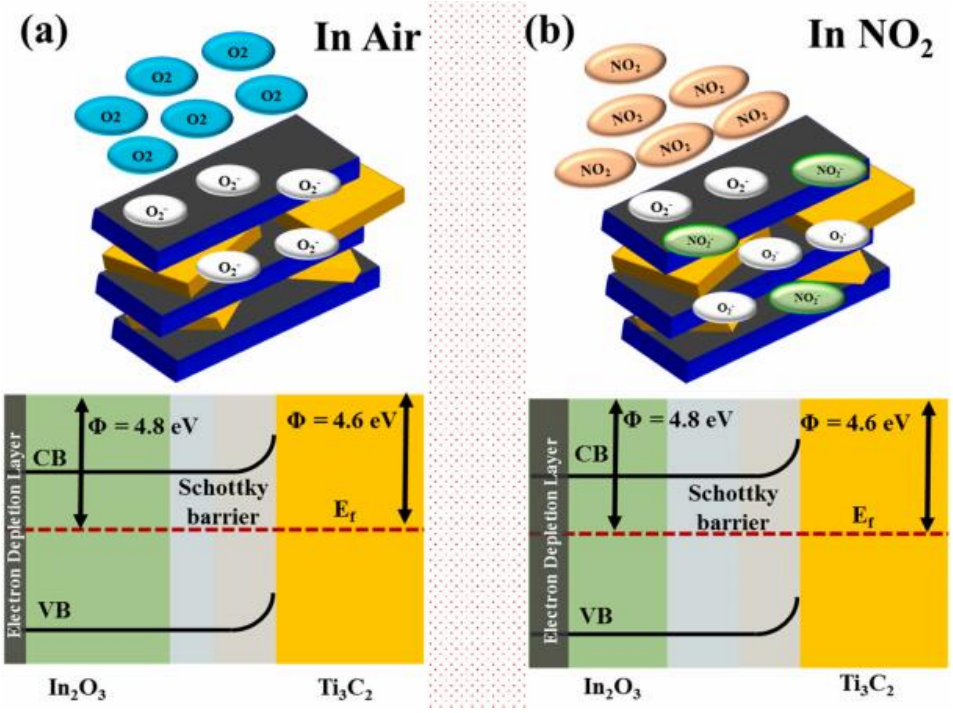


Figure 2. Diagram of gas-sensing mechanism and band structure of the In_2O_3/Ti_3C_2: (**a**) The surface nad band structure of In_2O_3/Ti_3C_2 in air [22]; (**b**) The surface nad band structure of In_2O_3/Ti_3C_2 in NO_2 [22].

Table 2. Comparison of the room-temperature NO_2 sensing performance of various 2D materials.

Sensing Material	Conc. (ppm)	Response Value (R_g/R_a or R_a/R_g)	Response/Recovery Time (s)	Reference
rGO/Bi_2S_3	1	9.8	22/106	[23]
rGO/CuO	5	11.04	10/110	[24]
rGO/CuO nanoflakes	5	1.26	6.8/55.1	[20]
vacancies-rich SnO_2-RGO	1	5.8	95/385	[25]
rGO/In_2O_3	1	1177	675/559	[21]
8 wt% GO-mediated In_2O_3	1	1021	413/182	[26]
In_2O_3/Ti_3C_2 nanosheets	100	371.19	18/95	[22]
$Ti_3C_2T_x$	10	1.14	-/-	[27]
$Ti_3C_2T_x$-sphere-like CuO	50	1.57	13.5/20.9	[28]
Ti_3C_2-I	120	1.15	90/105	[29]
$Ti_3C_2T_x/WS_2$	1	1.15	-/-	[30]
V_2CT_x/SnS_2	5	2.49	4.8/4.7	[31]
$MoSe_2$-WS_2	0.05	1.60	68.9/65.7	[32]
$GaSe_{0.58}O_{0.42}$	6	7.75	48/378	[33]
$MoSe_2$/0.5–Co_3O_4	0.05	1.26	139/20	[34]

Except for 2D materials, traditional metal oxides and sulfides are being explored for NO_2 sensing, offering high and fast responses. Notably, MoO_3@$CoMoO_4$@$CoMoS_{3.13}$ can respond to 40 ppm NO_2 in only 1.1 s, with a response value as high as 35.42 [35]. A possible NO_2 sensing mechanism was proposed as follows: (1) NO_2 is first absorbed onto the surface layer ($CoMoO_4$@$CoMoS_{3.13}$) of the nanocomposite containing S-modified vacancies to contact with Co sites. (2) The electron is then sucked by the NO_2 molecule and reacts with the chemisorbed oxygen ($2NO_2$ (gas) + O_2^- (ads) + $2e^- \rightarrow 2NO_3^-$ (ads)). (3) A full recovery of the resistance is accompanied with the removal of NO_2 from the sensing system, realizing the return of the electron to material. Recently, Zhang et al. found that $ZnInS_4$

can respond to 10 ppm NO_2 in only 2 s, with a response value of 3.28 [36]. The excellent room-temperature NO_2 sensing properties of $ZnInS_4$ may result from the presence of rich sulfur vacancies. The breakneck response/recovery speed is due to the open structure of $ZnIn_2S_4$/MIL-68(In), which promotes the adsorption and diffusion of NO_2 molecules.

Tellurium (Te), a 2D elemental material, is promising for NO_2 detection due to its suitable band structure for gas adsorption and charge mobility. However, Pure Te materials have poor stability due to their high activity, which limits their application in gas sensor fields. Core−shell 2D Te@Se heterostructures are prepared using a solvothermal method [37]. The Te@Se heterostructures with a thickness of 4–6 nm of Se demonstrate an exceptionally high response of 7.22 to 1 ppm of NO_2 at room temperature, with ultrafast response/recovery times of 10 s and 30 s, respectively. The room-temperature NO_2 sensing performance of Te@Se depends strongly on the thickness of the Se shell, as seen in Figure 3a–c. Three cases may happen: (1) When the Se shell is too thin, the electron accumulation layer in Se is smaller than the theoretical thickness, leading to a minimal electron migration effect and resistance modulation ability (as shown in Figure 3a); (2) When the thickness of the Se shell exceeds that of the electron accumulation layer, the electrons in the accumulation layer must pass through the Se shell to bind with NO_2 (Figure 3c), resulting in lower electron mobility in Se. Consequently, the efficient transfer of accumulated electrons to NO_2 is hindered. (3) The resistance modulation effect from electron migration is maximized only when the thickness of the Se shell matches that of the electron accumulation layer, as seen in Figure 3b. As a result, the highest NO_2 response can be achieved in this case. Furthermore, SnO_2-decorated Te nanotubes are found to respond to 600 ppb NO_2 in 32 s, with a response value of 1.33 [38]. The mechanism for enhanced sensor performance can be attributed to Schottky barriers, as shown in Figure 3d. When the material is exposed to NO_2, the adsorbed NO_2 can form adsorbed NO_2^- through either capturing electrons from SnO_2 decorated Te or reacting with surface O_2^-, as illustrated in Figure 3e. A detailed comparison of related materials can be found in Table 3.

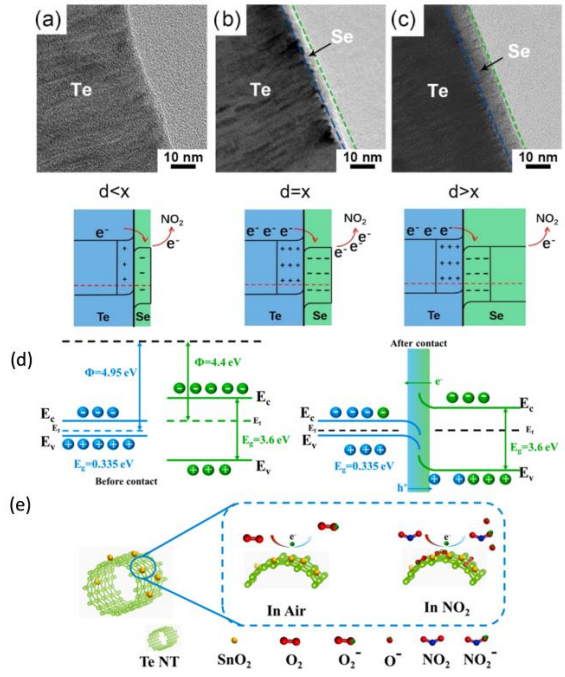


Figure 3. TEM images (top) and the corresponding heterojunction band structure (bottom) of Te@Se with different thicknesses of Se [37]: (**a**) Te@Se-1, (**b**) Te@Se-2, and (**c**) Te@Se-3; Schematic diagrams illustrating the gas-sensing mechanism of Te NT/SnO_2 [38]: (**d**) band structures of Te and SnO_2, (**e**) sensing process of the TeNT/SnO_2-based sensor.

Table 3. Comparison of the room-temperature NO_2 sensing performance of various non-2D materials.

Sensing Material	Conc. (ppm)	Response Value (R_g/R_a or R_a/R_g)	Response/ Recovery Time (s)	Reference
MoO_3@$CoMoO_4$@$CoMoS_{3.13}$	50	35.42	1.1/-	[35]
Te@Se Core−Shell	1	7.22	10/30	[37]
$ZnInS_4$	10	3.28	2/3.7	[36]
Hollow Co_3O_4 nanocages in NiO cilia	100	47.4	1.3/9.6	[39]
UV-activated p-type $CuCrO_2$	250	3.60	107/300	[40]
SnO_2 decorated Te nanotubes	0.6	1.33	32/109	[38]
Au@In_2S_3/In_2O_3	100	20.7	12/27	[41]

2.3. Room-Temperature H_2 Sensor

H_2 is attracting increasing attention due to its excellent properties, including high efficiency, cleanliness, and renewability. However, it has a relatively wide explosion limit (4~75%), causing a significant threat to human and city safety. Room-temperature H_2 sensing is particularly meaningful for avoiding the heating risk associated with the sensor itself [42–44]. Three-dimensional (3D) structure nanomaterial composites have been investigated for rapid room-temperature H_2 sensing. For example, Chen et al. successfully synthesized a 3D In_2O_3-rGO-PPy composite aerogel using a hydrothermal method [45]. It can respond to 1000 ppm H_2 in 13 s with a response value of 11.6. The mechanism is as follows: The oxygen gas will form chemisorbed oxygen ions (O_2^-) when oxygen molecules are adsorbed on the surface of the 3D In_2O_3-rGO-Ppy at room temperature. After H_2 exposure, the oxygen ions on the surface react with H_2 to form H_2O, as shown in Figure 4a.

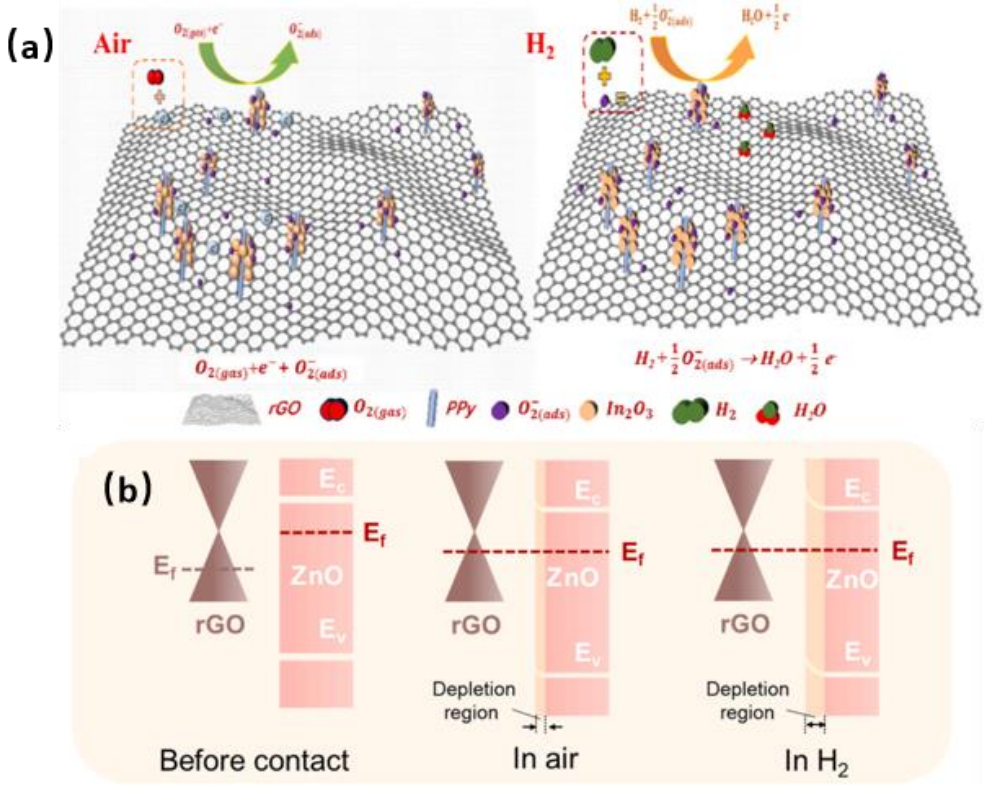


Figure 4. Gas-sensitive response mechanism of different 3D materials: (**a**) In_2O_3-rGO-Ppy [45]; (**b**) Cactus-like ZnO@3D rGA [46].

Furthermore, Cactus-like ZnO@three-dimensional reduced graphene oxide aerogels (Cactus-like ZnO@3D rGA) respond to 10,000 ppm H_2 in 15 s, achieving a response value of 81.07 [46]. The enhanced sensing performance is attributed to the p-n heterojunction between ZnO (n-type with a work function of 4.25 eV) and rGO (p-type with a work function of 4.86 eV), as shown in Figure 4b. When ZnO is in contact with rGO, electrons from ZnO will be transferred to rGO. In contrast, the holes in rGO will be transferred to ZnO in the opposite direction. The superior room temperature sensing behavior of ZnO-rGO toward H_2 can be attributed to two reasons: on the one hand, rGO can increase the conductivity of the composites and form a heterojunction with ZnO; on the other hand, 3D rGO possesses a pore structure, which facilitates the adsorption and desorption of gases. Additionally, the porous structure can increase the number of active sites for surface gas reactions. A summary of the performance of related materials is shown in Table 4.

Table 4. Comparison of the room-temperature H_2-sensing performance of various materials.

Sensing Material	Conc. (ppm)	Response Value (R_g/R_a or R_a/R_g)	Response/Recovery Time (s)	Reference
flower-like In_2O_3/SnS_2	1000	3.43	-/-	[47]
Mace-like In_2O_3@ZnO microtubules	10,000	6.67	178/338	[48]
5.0Pd@ZnO	200	1.53	-/-	[49]
Pd-Mg alloy thin films	500	1.13	85/360	[50]
3D In_2O_3@rGO@PPy aerogel	1000	11.6	13/29	[45]
Cactus-like ZnO@3D rGA	10,000	81.07	15/27	[46]
$MoSe_2$ -WSe_2	25	1.60	16/30	[51]

2.4. Room-Temperature CH_4 Sensor

Li et al. created Pt-doped SnO_2/ZnO bilayer structures showing CH_4 response at room temperature [52], attributed to the combined effects of n-n heterojunction and Schottky barrier, as depicted in Figure 5a. Optimal sensitive materials: 1.0Pt-SnO_2/ZnO exhibits prolonged response and recovery times exceeding 100 s for a 2000 ppm CH_4 concentration. Yang et al. designed In_2O_3-ZnO/laser-induced graphene composites for room-temperature CH_4 sensors, achieving a 27.48% response at 500 ppm CH_4 with response/recovery times of 48/169 s, respectively, and a detection limit as low as 3 ppm [53]. Li et al. prepared Ag-Ru co-doped ZnO nanorod arrays, enabling CH_4 detection at room temperature [54]. As seen in Figure 5b, the work function of ZnO is 4.44 eV, while that of Ag/ZnO and $AuRu_{0.025}$/ZnO is 4.51 and 5.03 eV, respectively. The Fermi level in Ag-ZnO contributes to the enhanced oxygen vacancy density, and that in $AuRu_{0.025}$-ZnO proves the role of p-type lattice defects. The localized contact between Ag-ZnO/$AuRu_{0.025}$-ZnO supports the experimental result that the electrons are transferred from the Ag−Ru co-doping site to the nearby Ag-doping site, reducing Ag^+ to Ag^0 in $AgRu_{0.025}$-ZnO. The localized contact between ZnO/Ag-ZnO reveals that more electrons accumulate in the Ag-doping sites, which act as activity sites for O_2 chemical adsorption.

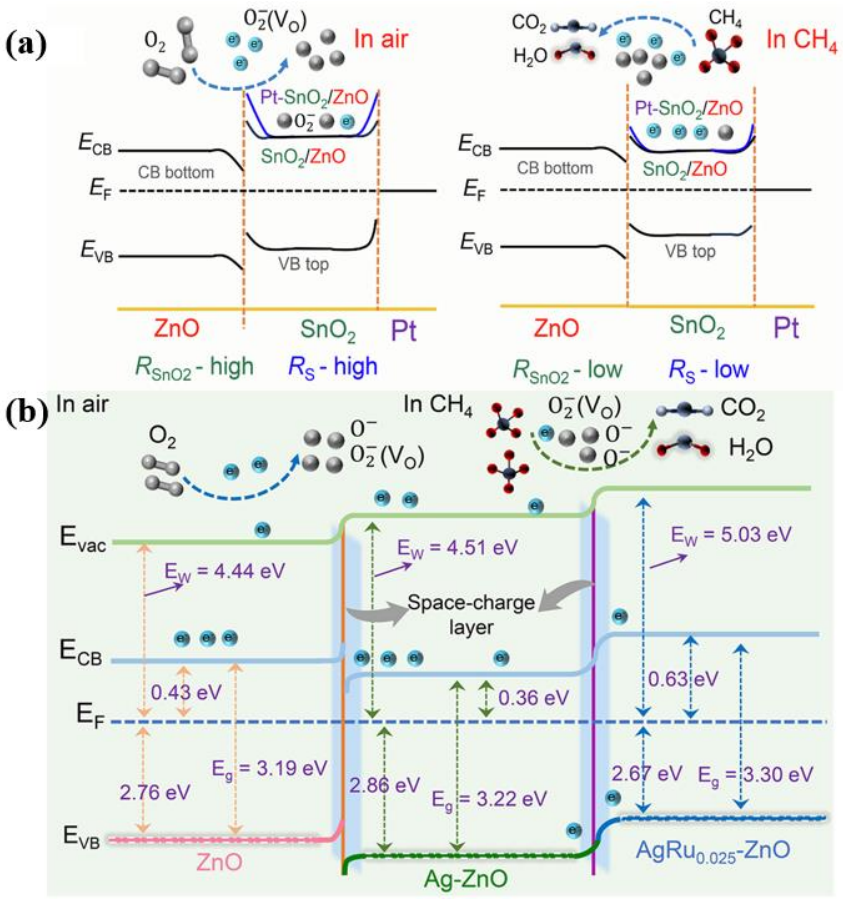


Figure 5. (**a**) Band structure and methane sensing mechanism of: (**a**) Pt-SnO_2/ZnO [52]; (**b**) AgRu/ZnO [54].

Detailed sensing information of related materials is presented in Table 5. To be noteworthy, UV light activation can be an effective route to enhance the methane sensing performance at room temperature [55,56]. For example, AuAg/ZnO can respond to 5000 ppm CH_4 in 5 s, with a response of 62.61 [56]. The conductivity of ZnO will increase under UV illumination since the electrons of ZnO will be excited from the valence band to the conduction band. Oxygen molecules will trap photogenerated electrons adsorbed on the ZnO surface, forming reactive oxygen species and creating an electron-depletion layer. Upon CH_4 exposure, CH_4 molecules react with oxygen ions, causing electrons to return to ZnO and reducing resistance.

Table 5. Comparison of the room-temperature CH_4 sensing performance of various materials.

Sensing Material	Conc. (ppm)	Response Value (R_g/R_a or R_a/R_g)	Response/Recovery Time (s)	Reference
Pt-SnO_2/ZnO	2000	3.73	150/147	[52]
In_2O_3−ZnO/Laser-Induced Graphene	500	1.38	48/169	[53]
Ag−Ru Co-doped ZnO Nanorods	800	1.8	-/-	[54]
Mulberry-Like ZnO/SnO_2 Hierarchical Structure	100	1.27	163/89	[57]
Photo-activated Au-modified ZnO microsphere	5000	4.65	-/-	[58]
UV-activated ZnO spheres	1000	10.18	6/134	[55]
UV-activated AuAg/ZnO	5000	62.61	5/-	[56]
NiO/ZnO	5000	8.61	32/182	[59]
MWCNT with MOF (PCN-14)	50,000	-	120/-	[60]
MWCNT/Pd	100	1.36	20/25	[61]

To summarize, despite significant advancements in related research, several practical application shortcomings persist for this type of sensor, including susceptibility to humidity, prolonged response times, reduced sensitivity to low gas concentrations, and poor selectivity for target gases. It is not competitive enough in scenarios with high requirements on stability and sensitivity.

3. MEMS Gas Sensor

MEMS sensors, based on microelectromechanical systems (MEMS) technology, are typically compact (1 μm to 1 mm in size) and feature unique manufacturing processes that enable the easy construction of gas sensing arrays or grids. These sensors offer several significant advantages, including high sensitivity, rapid response times, low power consumption, and easy integration. By developing and refining sensitive materials with varying characteristics, they can effectively detect different gases. Hadano et al. developed a MEMS catalytic combustion CH_4 gas sensor featuring platinum-loaded catalysts as reference elements to enhance methane selectivity, while improving CH_4 sensitivity through structural modifications, such as enhancements to the micro-thermal plate design [62]. Yang et al. fabricated a quadri-lateral MEMS MOS gas sensor cell with four different sensitive materials based on a complete semiconductor process, as seen in Figure 6a–d. Jang et al. designed a MEMS catalytic combustion micro-gas sensor for leak detection [63]. Measuring just 3 mm × 3 mm, this sensor achieves an output voltage of 0.29 mV at 1158 ppm CH_4 and 104 mW of input power, demonstrating both low power consumption and excellent selectivity.

MEMS catalytic combustion sensors exhibit relatively high power consumption and are susceptible to poisoning effects. In contrast, MEMS metal oxide sensors offer several advantages, including lower-power consumption, higher sensitivity, lower detection limits, greater material modification potential, and improved stability. Yan et al. designed an intelligent MEMS sensor based on FeCoNi oxidation of an entropy alloy, which reduces power consumption via a pulse-heating mode [64]. At 150 °C, it shows excellent selectivity for H_2 and CO with detection limits of 0.3 ppm and 0.29 ppm, respectively. Yang et al. made a quadrilateral MEMS metal oxide gas sensor cell with four different sensitive materials based on a complete semiconductor process, as shown in Figure 6a–d [65]. Li et al. proposed a MEMS CO sensor based on SnO_2 nanosheets, as shown in Figure 6e,f [66]. Figure 6g compares the sensor's response to CO under constant-temperature and pulse-heating modes, revealing a response of 34.3 at 200 ppm CO in pulse mode—1.56 times that in the constant-temperature mode—with approximately 19.8 mW of power consumption. Luo et al. developed a single MEMS sensor based on SnO_2 nanosheets [67]. At 370 °C, this sensor achieves a response of 297.7 ppm to H_2, with power consumption as low as 26.6 mW in pulse-heating mode. Wu et al. proposed a H_2 sensor based on Pd-loaded SnO_2 nanofibers, demonstrating an excellent response to 200 ppm H_2 at 185 °C (Figure 6h), with a power consumption of only 9.1 mW [68]. Figure 6i compares the response values of self-made S1, S2, and S3 sensors with those of the commercial MICS-5524 sensor at 185 °C for H_2 concentrations ranging from 200 to 8000 ppm, showing that the self-made sensors outperform the commercial sensor at high concentrations. Li et al. proposed a MEMS differential thermoelectric stack hydrogen sensor with response and recovery times of 14 s and 10 s, respectively, at 400 ppm H_2, and a power consumption of only 61 mW [69].

In summary, MEMS metal oxide gas sensors achieve rapid response to target gases with low power consumption in gas detection by integrating micro-structured designs with suitable sensitive materials. Current research on low-power-consumption MEMS metal oxide gas sensors primarily focuses on two aspects: First, optimizing the sensor's micro-hotplate structure—high thermal conductivity silicon-based microstructures reduce

heat loss and lower power consumption while maintaining appropriate temperatures. Second, improving sensitive materials through nanostructuring to enhance specific surface area for gas adsorption efficiency, or constructing composite metal oxide systems to optimize selectivity and stability while reducing baseline drift during prolonged operation. These synergistic advancements collectively reinforce the core advantages of MEMS sensors—"low power consumption, high responsiveness, and miniaturization"—forming an essential foundation for functional and performance breakthroughs.

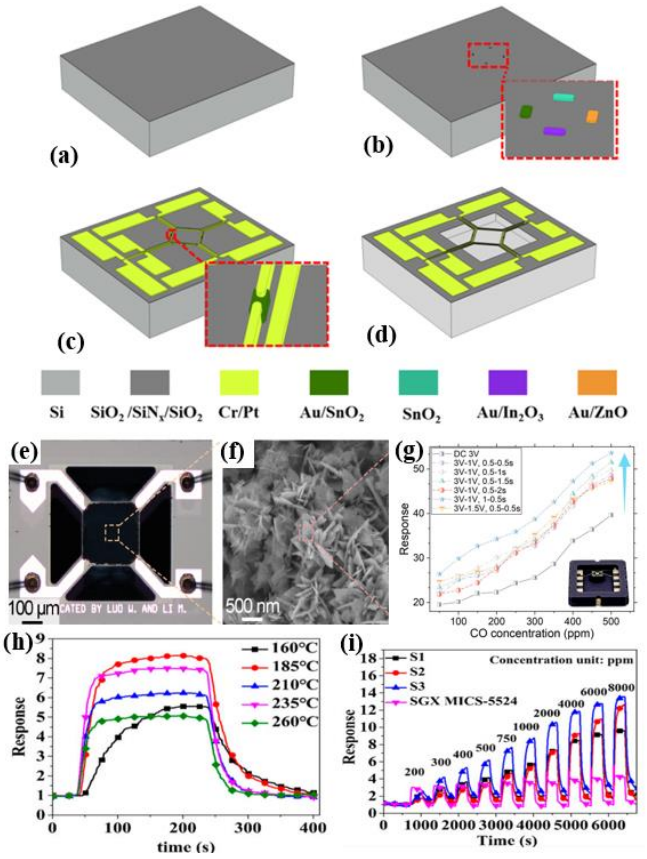


Figure 6. (**a**–**d**) Fabrication steps of the proposed gas sensor cell [65]: (**a**) Supporting layer by LPCVD; (**b**) Four sensing material deposition and patterning; (**c**) Heater and detecting electrodes patterning; (**d**) Dry-etching processes for releasing suspended structures. (**e**) Optical image of the SnO_2 nanosheet on the MEMS hotplate [66]; (**f**) SEM of the SnO_2 nanosheet on the MEMS hotplate [66]; (**g**) Sensor response to CO under different modes (constant temperature vs. pulse heating [66]). (**h**) Response of Pd-loaded SnO_2 nanofiber sensors at 2000 ppm H_2 exposure under varying temperatures [68]; (**i**) Dynamic response curves of three S1, S2, and S3 labeled SnO_2 nanofiber MHP gas sensors to H_2 [68].

3.1. Research Progress of MEMS Micro Hotplate

A micro hotplate (MHP) is a crucial component in MEMS gas sensors. It is based on silicon microfabrication technology, and its basic structure includes a silicon substrate, a suspended distributed support film, and a heater electrode. The power consumption of MHP is mainly affected by its materials and structure.

Yang et al. proposed a novel multi-heater MHP design based on thermal coupling [70]. Figure 7a shows the planar schematic of a dual-heater MHP, where heaters with a 100 μm radius achieve excellent temperature uniformity at 300 °C. The thermal coupling effect significantly reduces MHP power consumption, saving approximately 4.68 mW compared to single-heater configurations. Figure 7b illustrates the temperature distribution in MHPs with and without etched windows. The etched window design leverages air's superior

thermal insulation, increasing peak temperatures by about 40 °C while effectively reducing heat loss. Zhang et al. developed an MHP for wafer-level packaging of MEMS gas sensors using an ONO composite layer as support [71]. By analyzing different heater electrode shapes and cantilever beam materials, they found that serpentine electrodes produced the most uniform temperature distribution. The optimized MHP exhibits lower power consumption and enables the high-density integration of multiple independent, temperature-controlled MHPs.

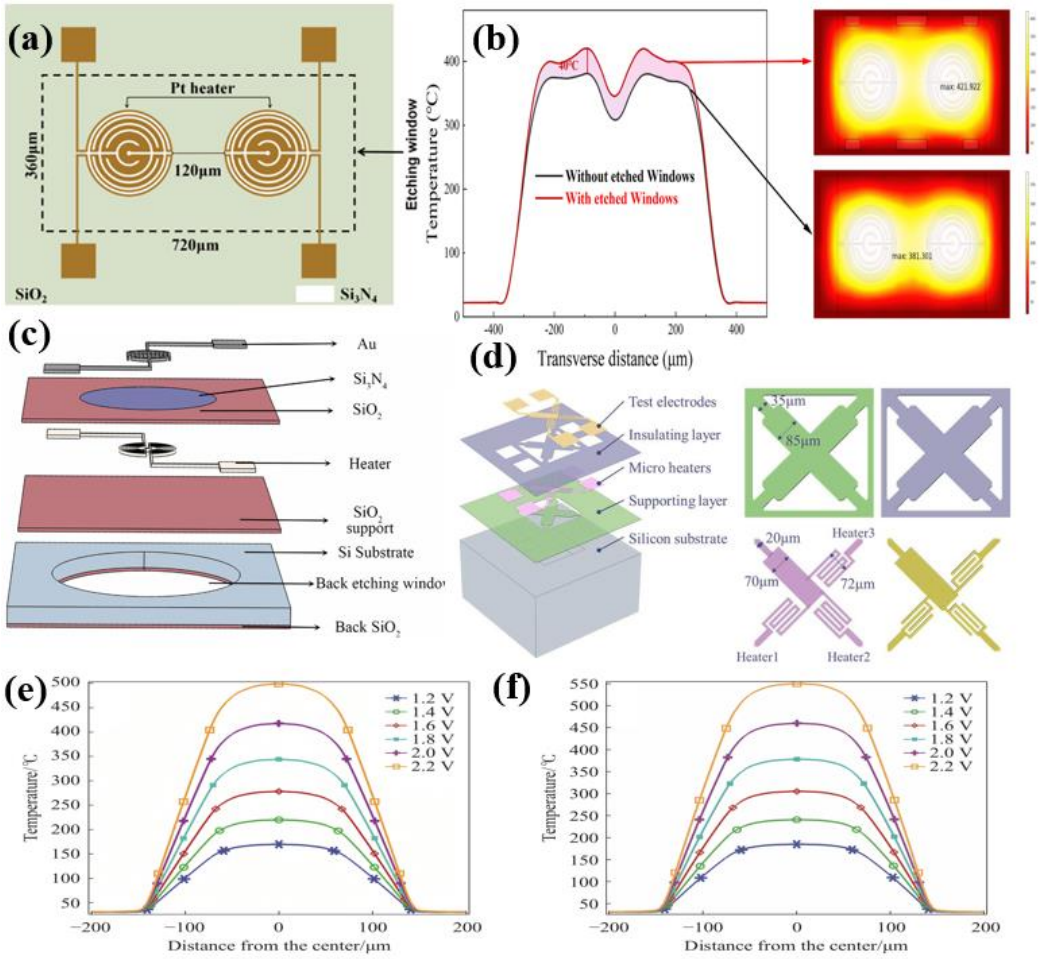


Figure 7. (**a**) Schematic diagram of the planar configuration of the thermal quenching heater MHP [70]; (**b**) Temperature distribution of MHP with and without etched windows [70]; (**c**) Structural schematic of Si_3N_4-SiO_2 composite dielectric layer MHP [72]; (**d**) Three-micro-thermal-plate integrated array structure MHP [73]; The temperature distributions under different heating voltages for structures 1 and 2 designed by our research group are shown as follows: (**e**) Structure 1 [74]; (**f**) Structure 2 [74].

Wei et al. introduced a planar MHP design combining Si_3N_4-SiO_2 lateral composite dielectric layers with annular heaters (Figure 7c) [72]. The composite dielectric layer effectively reduces lateral heat conduction losses and mitigates mechanical deformation in planar microheat plates. Zhang et al. created a novel MHP array structure integrating three MHPs per suspended region (Figure 7d) [73]. This configuration enhances integration density and achieves independent temperature control. Using COMSOL simulations, they optimized the platinum heater thickness and adjusted the cantilever and electrode widths, effectively reducing crosstalk interference. We conducted finite-element analysis of two serpentine MHP platinum electrode configurations. Structure 1 features identical heating electrode width and spacing, while Structure 2 maintains uniform spacing but exhibits a

gradually increasing micro-heater width from both sides toward the center. Figure 7e,f display temperature variations under different heating voltages for structures 1 and 2. Through COMSOL simulation analysis, it was found that under equivalent power consumption, Structure 2 demonstrates slightly higher maximum central temperature than Structure 1, while achieving lower power consumption at the same temperature levels [74].

Multiple researchers have optimized MHP structures by integrating heaters, selecting appropriate support layers and electrode configurations, introducing composite dielectric layers, and designing arrays. These optimizations have demonstrated significant improvements in power efficiency, stability, selectivity, and integration density, providing diverse approaches for related optimization and applications. However, limitations remain: precise control of multi-heater thermal crosstalk may compromise detection accuracy; etching windows and composite dielectric layers could reduce structural strength, increasing fracture risk; cross-interference in arrays remains challenging to eliminate; and some designs involve complex processes that increase mass-production costs. These issues highlight the need to strike a better balance between structural stability, thermal interference control, and process simplification.

3.2. MEMS MOS Sensors Based on Various Sensitive Materials

In view of the problems encountered by MEMS gas sensors in practical applications, such as low response values and poor selectivity, this paper will summarize and analyze a series of MEMS gas sensors with excellent performance by further optimizing the sensitive materials for CO, NO_2, CH_4, and H_2.

3.2.1. MEMS MOS CO Sensors

Carbon monoxide (CO), a primary hazardous gas in coal mines, originates from the spontaneous combustion of coal in mined-out areas and the incomplete burning of coal dust during mine gas explosions. This highly toxic, combustible substance can rapidly cause fatal consequences. Low-power-consumption CO sensors serve as critical safeguards for safe coal mining operations and form the essential foundation for distributed wireless sensing technologies. Comparison of the sensing performance of various MEMS MOS CO sensors can be found in Table 6.

In recent years, MEMS-based CO sensors have garnered significant attention in the field. Kim et al. synthesized Pd-SnO_2 nanoscale powders as CO gas sensors using the sol–gel method, as shown in Figure 8a [75]. In CO-NH_3 mixed gases, CO exhibits significantly higher sensitivity than NH_3, with Pd catalyzing CO adsorption and reactions that dominate the changes in sensitivity. The CO response is highly humidity-dependent, as illustrated in Figure 8b. Moon et al. developed a MEMS CO gas sensor by co-precipitating 10 wt% WO_3 and 0.5 wt% Pt-doped SnO_2 nanosheets [76]. This sensor consumes approximately 15 mW of power and detects CO at concentrations as low as 2 ppm. It shows a response value of about 1.31 at 20 ppm CO, with response and recovery times of 91 s and 134 s, respectively. Egger et al. developed a MEMS gas sensor based on SnO2 films, utilizing Ag, Pd, Ru, and their combinations as catalysts to enhance CO sensitivity while mitigating humidity-induced cross-sensitivity [77]. The sensor operates effectively at 200 °C and responds to CO and hydrocarbon mixtures ranging from 5 to 50 ppm. As shown in Figure 8c, the AgRu- and AgPd-functionalized sensors exhibit high CO sensitivity with low humidity cross-sensitivity. In contrast, the tri-metal PdAgRu-functionalized sensor exhibits the strongest CO response (Figure 8d). Vanmathi et al. optimized the fabrication parameters for Al-doped TiO_2 films via radio-frequency magnetron sputtering [78]. The increased surface area provides more active sites for gas absorption, significantly altering

the material's resistivity. The sensor has a detection limit of 55% at a CO concentration of 200 ppm.

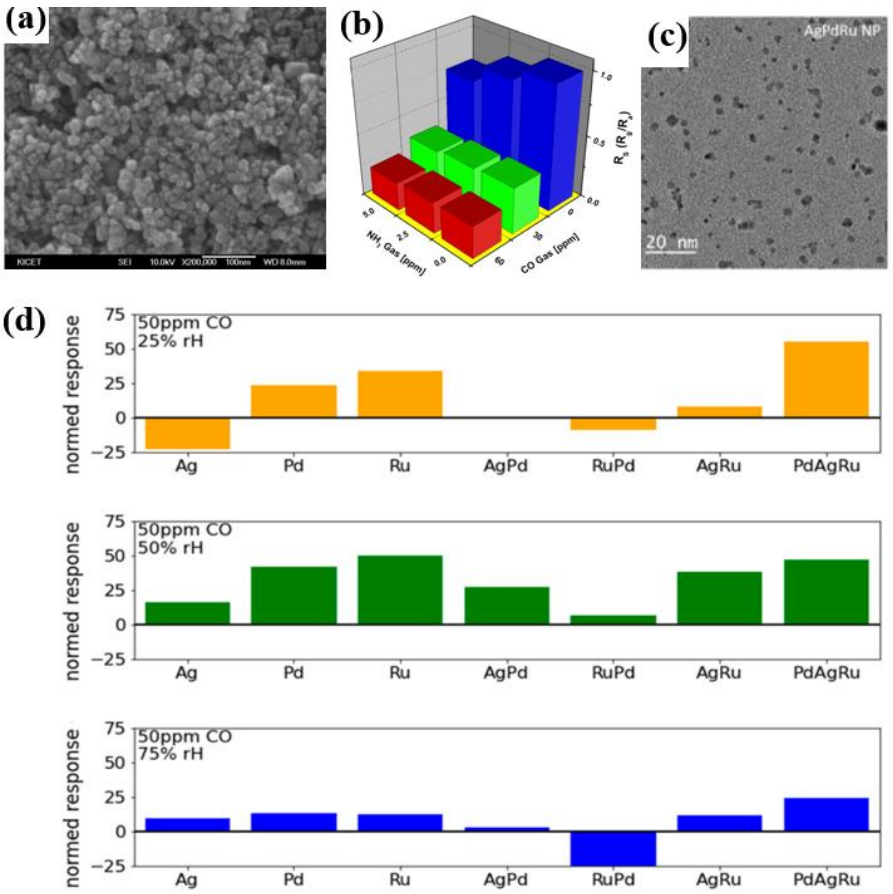


Figure 8. (**a**) SEM image of Pd-SnO_2 nanomaterials [75]; (**b**) 3D bar chart of gas sensitivity characteristics of Pd-SnO_2 sensors in CO-NH_3 gas system [75]; (**c**) TEM image of the three-metal PdAgRu structures [77]; (**d**) Normalized response of different SnO_2 composites toward 50 ppm CO at various humidity levels [77].

Table 6. Comparison of the sensing performance of various MEMS MOS CO sensors.

Sensing Material	Working Temperature (°C)	Conc. (ppm)	Response Value (R_g/R_a or R_a/R_g)	Response/ Recovery Time (s)	Reference
10 wt%WO_3/0.5 wt%Pt/SnO_2 NS	400	20	1.31	91/134	[76]
Ag/Pd/Ru/SnO_2	200	50	1.67	-/-	[77]
Al doped TiO_2	400	200	2.22	-/-	[78]
Pd/SnO_2 nanopowder	300	60	0.23	-/-	[75]

3.2.2. MEMS MOS NO_2 Sensors

Recently, MEMS MOS sensors have been explored for NO_2 sensing, due to their high response, fast detection speed, and ease of integration. For example, Hsueh first synthesized Co_3O_4 nanoparticles (NPs) through ultrasonic wave grinding and then decorated the Co_3O_4 with Au NPs [79]. The Au/Co_3O_4-NPs MEMS gas sensor exhibits higher sensitivity to NO_2 than to other gases (SO_2, NH_3, CO) at an optimal operating temperature of 136 °C. Comparison of the sensing performance of various MEMS MOS NO_2 sensors can be found in Table 7.

Table 7. Comparison of the sensing performance of various MEMS MOS NO_2 sensors.

Sensing Material	Temperature (°C)	Conc. (ppm)	Response Value (R_g/R_a or R_a/R_g)	Response/Recovery Time (s)	Reference
Au-Co_3O_4 NPs	136	0.1	1.34	84/68	[79]
CuO NWs	110	0.5	2	-/-	[80]
ZnO nanopowder	200	10	41.6	41/-	[81]
Hierarchically porous ZnO	190	10	3.42	9/26	[82]
Oxygen-enriched SnO_2 NPs	102	0.5	14.7	45.9/178.2	[83]

CuO nanowires (NWs) can be produced through RF sputtering and integrated with a MEMS structure to form a MEMS sensor [80]. The sensor can detect 500 ppb NO_2, with a response value of 1.63 at 131 °C. ZnO nanomaterial was deposited on a ceramic MHP by a microextruder [81]. The MEMS sensor has a response value of 41.6 toward 10 ppm NO_2 at 200 °C. Meanwhile, Xu et al. obtained hierarchically porous ZnO by annealing Zeolitic Imidazolate Frameworks (ZIF-90) at 450 °C [82]. The optimal MEMS sensor can detect 10 ppm NO_2 in 9 s with a high response. In addition, tiny SnO_2 NPs with enriched oxygen vacancies are synthesized through the hydrothermal method assisted by PVP. The obtained SnO_2 NPs are employed in MEMS gas sensors, which can have a response value of 14.5 toward 500 ppb NO_2 at 102 °C in 45.9 s [83]. The superior gas-sensing performance of the SnO_2 NO_2 sensor can be attributed to the effect of oxygen vacancies, which will introduce multiple midgap states or donor energy levels between the valence and conduction bands of the sensing material, accelerating the excitation of hot electrons into the conduction band. This process facilitates the adsorption of more NO_2 molecules onto the surface, where they rapidly capture electrons and subsequently participate in redox reactions, ultimately enhancing the gas-sensing performance, as shown in Figure 9a,b. Furthermore, doping with an appropriate amount of N not only increases the number of O_2^- species, providing additional active sites for NO_2 adsorption, but also enhances the electron-transfer rate, thereby improving carrier mobility in tin dioxide.

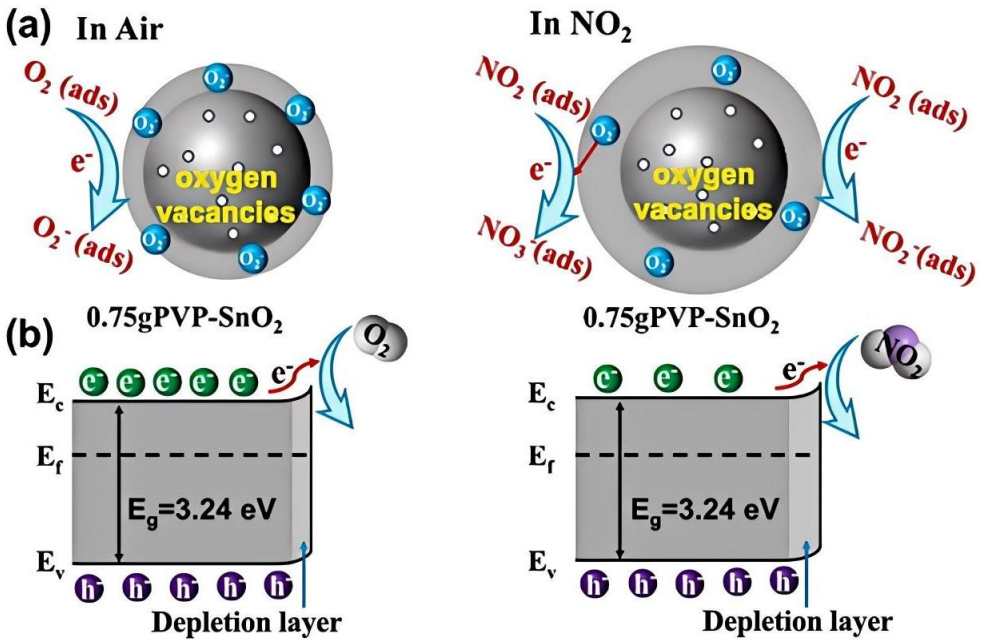


Figure 9. Gas sensing mechanism of oxygen-enriched SnO_2 NPs before and after exposure to NO_2 [83]: (**a**) Diagram of the gas-sensing mechanism; (**b**) Energy band structure and electron transfer.

3.2.3. MEMS MOS H_2 Sensors

H_2 is a highly flammable gas with an extensive explosive limit (4–75% in air). A leak mixed with air can easily ignite upon exposure to open flames or static electricity, potentially causing explosions or fires. H_2 sensors enable real-time concentration monitoring and trigger alarms when concentrations approach hazardous thresholds, preventing safety incidents. In recent years, MEMS hydrogen sensors have achieved remarkable advancements in research.

Comparison of the sensing performance of various MEMS MOS H_2 sensors can be found in Table 8.

Table 8. Comparison of the sensing performance of various MEMS MOS H_2 sensors.

Sensing Material	Working Temperature (°C)	Conc. (ppm)	Response Value (R_g/R_a or R_a/R_g)	Response/Recovery Time (s)	Reference
Pt/Nb-doped TiO_2 nanoplate	40	1000	12.3	30/270	[84]
rGO/Nb-doped TiO_2-nanoplate	100	1000	2.5	32.5/58	[85]
PdNPs@Al_2O_3	200	400	-	14/10	[69]
oxygen vacancy-enhanced SnO_2	250	6	2.3	7/12	[86]
Pd-SnO_2 nanoflower clusters with F-WO_3 microparticles	300	15	18.7	10/22.5	[87]

Zhang et al. developed a Pt-modified 0.4% Nb-doped TiO_2-nanoplate MEMS hydrogen sensor that achieves 12.3 Hz response at room temperature for 1000 ppm H_2, with response and recovery times of 31 s and 270 s, respectively, demonstrating excellent selectivity, stability, and repeatability [84]. He et al. created a reduced graphene oxide (rGO)-modified Nb-doped TiO_2-nanoplate MEMS H_2 sensor, where 10% rGO and 0.8% Nb-doped TiO_2-nanoplates showed a 2.5 Hz response at 100 °C for 1000 ppm H_2 with response/recovery times of 32.5/58 s [85]. Luo et al. [86] introduced an oxygen vacancy-enhanced SnO_2 (SnO_2-D) MEMS H_2 sensor, where D4 modification altered the SnO_2 microstructure while regulating electronic states and gas adsorption reactions, optimizing target gas adsorption, dissociation, and electron transfer to enhance gas-sensitive response performance, as shown in Figure 10a. At the optimal operating temperature of 250 °C, the SnO_2-D4 sensor demonstrates a response value of 2.3 to 6 ppm H_2, surpassing the original SnO_2 (1.13). The response time and recovery time for six ppm H_2 are approximately 7 s and 12 s, respectively, as shown in Figure 10b. Li et al. proposed a gas sensor array by integrating Pd-SnO_2 nanoflower clusters with F-WO_3 microparticles on low-power-consumption microthermal plates, as illustrated in Figure 10c,d [87]. Operating at 300 °C (17 mW power consumption), it exhibits high sensitivity and low cross-sensitivity to eight gases, including H_2 and ammonia, as well as their mixtures. The Pd-SnO_2 nanoflower cluster exhibits an excellent linear response across H_2 concentrations ranging from 15 to 500 ppm, as shown in Figure 10e.

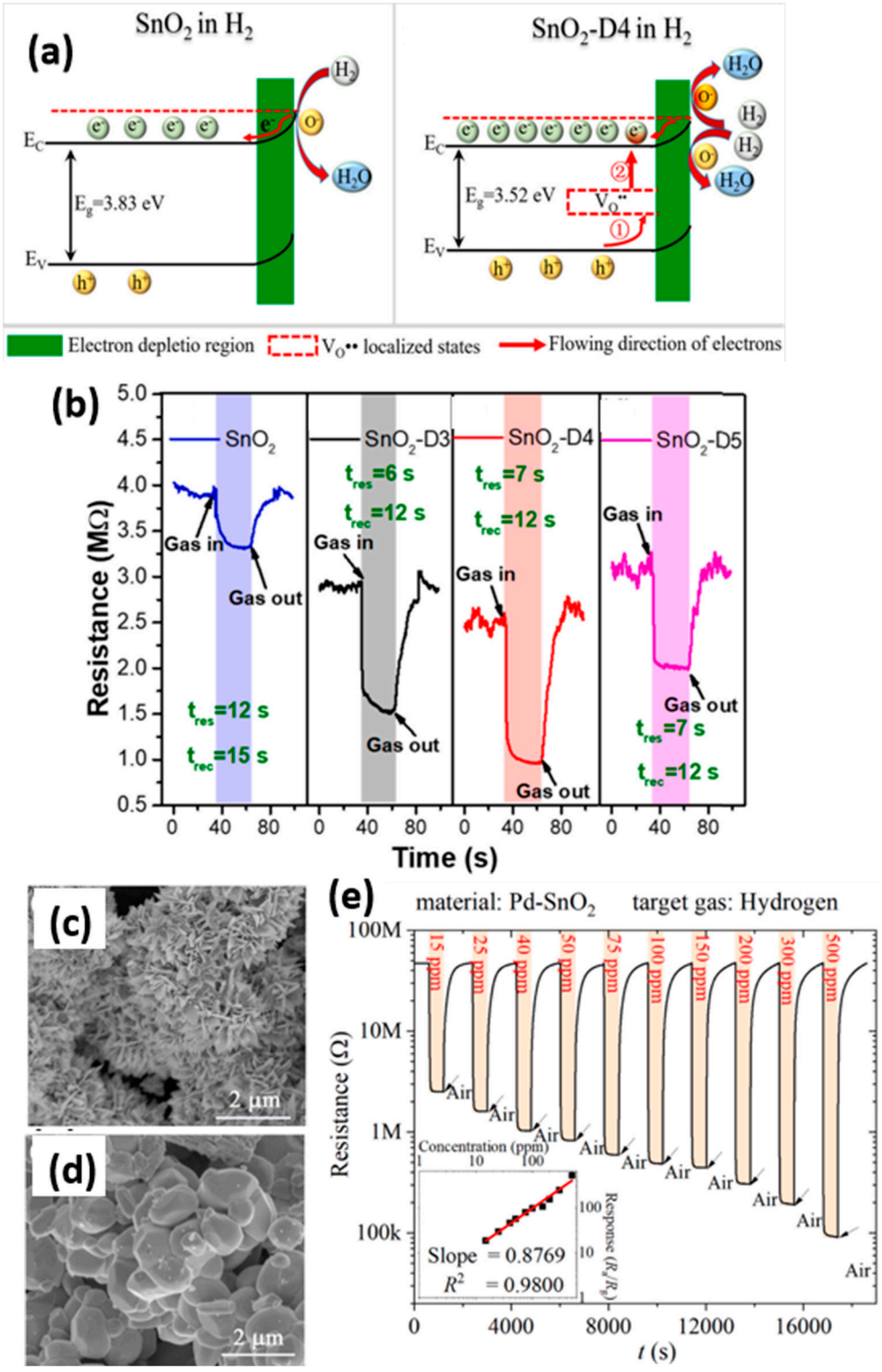


Figure 10. (**a**) Schematic diagrams of electronic structures and gas-sensitive response mechanisms for SnO_2 and SnO_2-D4 under H_2 environment [86]; (**b**) The dynamic responses of different SnO_2 samples, SnO_2-D3/SnO_2-D4/SnO_2-D5 refers to SnO_2 calcinate at 300/400/500 °C in H_2 atmosphere [86]; (**c**) SEM image of Pd-SnO_2 [87]; (**d**) SEM image of Pd-WO_3 [87]; (**e**) The dynamic responses of Pd-SnO_2 [87].

3.2.4. MEMS MOS CH_4 Sensors

CH_4, being a flammable and explosive gas, can easily cause fires or explosions, making real-time concentration monitoring crucial. The research on MEMS CH_4 sensors has

attracted increasing attention. Sagitova et al. synthesized Nb and Cr-doped SnO_2 gas sensing materials via flame spray pyrolysis [88]. Figure 11a shows the TEM image of SnO_2-Cr1Nb1 material, where hetero-doping reduced the response attenuation by half compared to pure SnO_2, with a response range of 100–400 °C for CH_4 pairs, as seen in Figure 11b. Niu et al. [89] fabricated MOS gas sensors based on Si/SiO_2-doped flexible fiber substrates, achieving CH_4 detection through the in situ synthesis of Co-doped ZnO nanorods on the fiber surfaces. The sensor exhibited a maximum response of 16% at 1000 ppm CH_4 under an optimal operating temperature of 50 °C, with a power consumption of 3.2 mW/mm^2 and response/recovery times of approximately 350 s/106 s, respectively. Li et al. modified SnO_2 nanosheets with PdPt bimetallic nanoparticles enriched in Pd shells and Pt cores to construct MOS gas sensors [90]. Figure 11c displays the TEM image of the 1P-PdPt/SnO_2-A material, which exhibits temperature-dependent dual selectivity, responding at 320 °C, with a peak response value of 5.2 for 1000 ppm CH_4. Figure 11d shows the gas response of 1P-PdPt/SnO_2 at 100/320 °C, demonstrating high selectivity for CH_4. Murata et al. developed MEMS gas sensors containing 7.5 at% Pt/SnO_2 thin-film catalysts [91]. The dispersed Pt atoms in this sensor maintain a stable SnO_2 lattice configuration. Under reducing gas and 703 K reaction conditions, minimal oxygen loss from the surrounding lattice occurs without Pt aggregation. The oxygen deficit is readily restored by air oxidation, ensuring high methane sensitivity and a long service life, with detection capability up to 12,500 ppm CH_4. A detailed comparison of different MEMS CH_4 sensors is presented in Table 9.

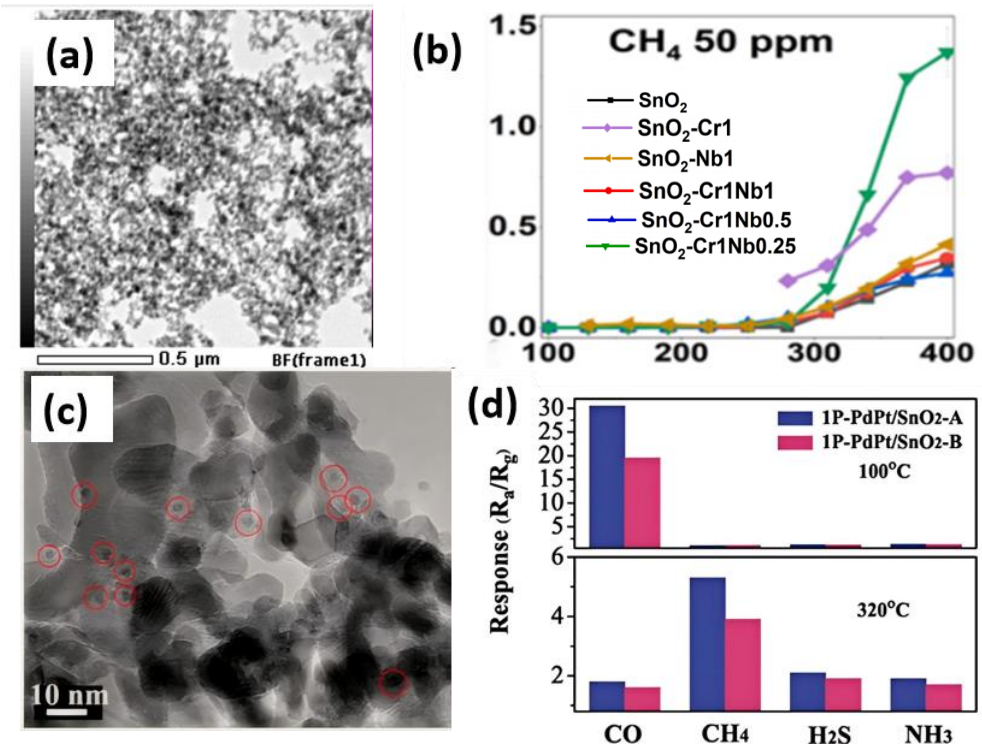


Figure 11. (**a**) TEM image of SnO_2-Cr1Nb1 material [88]; (**b**) Time-dependent response of gas sensors [88]; (**c**) TEM image of 1P-PdPt/SnO_2-A, red dots refer to PtPt bimetal [90]; (**d**) Response spectra of 1P-PdPt/SnO_2-A to different gases at 100/320 °C conditions [90].

Table 9. Comparison of the sensing performance of various MEMS MOS CH_4 sensors.

Sensing Material	Working Temperature (°C)	Conc. (ppm)	Response Value (R_g/R_a or R_a/R_g)	Response/Recovery Time (s)	Reference
Nb and Cr-doped SnO_2	400	50	3.35	-/-	[88]
Co-doped ZnO nanorods	50	1000	1.19	350/106	[89]
PdPt/SnO_2	320	1000	5.2	-/-	[90]
7.5 at% Pt-SnO_2 thin-film	430	12,500	-	-/-	[91]

4. Challenges and Prospects

Room-temperature gas sensors have attracted increasing attention in recent years, particularly due to their safety requirements and low power consumption. However, humidity and response speed are the primary concerns. Humidity effect can be alleviated through several routes: (1) surface decoration through functional materials, such as a catalytic filter or graphite [92,93]; (2) temperature modulation method [94]; (3) algorithm correction [95]. Surface decoration can provide reasonable protection against water vapor, though it may affect response speed if the coating is too thick. It will incur additional costs due to the addition of a functional substance. Algorithm correction has now become a hot topic in the humidity suppression area [96]. It has been shown in the previous section that fast gas response dynamics can be achieved by carefully tuning the material component and structure, as shown in [41,45].

The selectivity problem appears to be a universal issue for all MOS sensors, whether they operate at room or elevated temperatures, regardless of whether they use MEMS technology. It is due to the sensor's surface reaction-based principle. Advanced algorithms, combined with sensor array design, can be a suitable solution for this issue [97]. There are two general routes for data processing algorithms: machine learning and deep learning. Machine learning algorithms have better Interpretability than deep learning ones, but they require manual feature extraction and are easily influenced by environmental noise and fluctuations. Deep learning algorithms have high tolerance to environmental fluctuations and high recognition accuracy. It can automatically extract deep features from the data, despite typically having more complex network structures and poor interpretability [98]. Recently, Convolutional neural networks, ResNet, LSTM, and Transformer algorithms have been applied to gas recognition, achieving ideal results [99–101]. Furthermore, multi-task learning frameworks have been investigated for the dual tasks of gas classification and concentration regression [102–105]. Temperature modulation is another way to address the problem of selectivity [106,107]. Recently, our group also investigated the temperature modulation method and combined it with an FPGA to achieve the classification of seven different types of gases [108].

The stability of MOS gas sensors is very critical for their practical application. A recent review provides several routes for improving the stability of MOS gas sensors [109]. Firstly, p-type material may be superior in humidity resistance [110]. It is due to the surface metal cations' effect, i.e., facilitating strong oxygen adsorption and redox cycles, thereby inhibiting interference from water molecules. Secondly, hydrophobic modification with PDMS or rare-earth oxides can improve the interaction of water molecules [111,112].

5. Conclusions

This paper focuses on low-power-consumption metal oxide gas sensors for secure IoT applications, presenting research advancements in both room-temperature and MEMS gas sensors. Room-temperature gas sensors that operate without heating feature low power consumption and simple structures; however, they suffer from humidity sensitivity, slow response times, limited sensitivity to low-concentration gases, and limited selectivity. MEMS

gas sensors excel in high sensitivity, rapid response, low power consumption, and ease of integration. Their low-power-consumption operation is achieved through optimized microthermal plate structures and improved sensitive materials, demonstrating outstanding performance in detecting CH_4, H_2, NO_2, and CO. However, MEMS sensors face several challenges, including difficulties controlling thermal crosstalk, risks to structural integrity, and high production costs due to the complexity of their manufacturing processes. Future efforts should focus on enhancing room-temperature sensor performance (especially in selectivity and speed), promoting collaborative innovation in MEMS sensor structures and materials, and advancing intelligent, integrated solutions tailored for practical applications. A selectivity problem exists in both types of MOS gas sensors due to their working principles. Recent progress in advanced algorithms can provide an ideal solution for the selectivity problem.

Author Contributions: Conceptualization, Y.Z. and M.J.; methodology, M.J.; software, R.L.; validation, R.L., G.W. and Z.Z.; formal analysis, M.J.; investigation, R.L.; resources, Z.Z.; data curation, R.G.; writing—original draft preparation, Y.Z.; writing—review and editing, M.J.; visualization, R.L.; supervision, M.J.; project administration, G.W.; funding acquisition, Y.Z. All authors have read and agreed to the published version of the manuscript.

Funding: This research was funded by the National Science Foundation Council (52404266, 62204260), the Basic Research Program of Jiangsu (No. BK20241645), China Postdoctoral Science Foundation (2025T180510, 2024M753532), and Jiangsu Postdoctoral Science Foundation (2024ZB449).

Data Availability Statement: No new data were created or analyzed in this study. Data sharing is not applicable to this article.

Conflicts of Interest: The authors declare that they have no conflicts of interest.

References

1. Gao, D.H.; Yu, Q.C.; Kebeded, M.A.; Zhuang, Y.Y.; Huang, S.; Jiao, M.Z.; He, X.J. Advances in Modification of Metal and Noble Metal Nanomaterials for Metal Oxide Gas Sensors: A Review. *Rare Met.* **2025**, *44*, 1443–1496. [CrossRef]
2. Shooshtari, M.; Vollebregt, S.; Vaseghi, Y.; Rajati, M.; Pahlavan, S. The Sensitivity Enhancement of TiO2-Based VOCs Sensor Decorated by Gold at Room Temperature. *Nanotechnology* **2023**, *34*, 255501. [CrossRef]
3. Shooshtari, M.; Salehi, A. An Electronic Nose Based on Carbon Nanotube -Titanium Dioxide Hybrid Nanostructures for Detection and Discrimination of Volatile Organic Compounds. *Sens. Actuators B Chem.* **2022**, *357*, 131418. [CrossRef]
4. Jiao, M.; Zhao, X.; He, X.; Wang, G.; Zhang, W.; Rong, Q.; Nguyen, D.H. High-Performance MEMS Oxygen Sensors Based on Au/TiO2 Films. *Chemosensors* **2023**, *11*, 476. [CrossRef]
5. He, Y.; Jiao, M. A Mini-Review on Metal Oxide Semiconductor Gas Sensors for Carbon Monoxide Detection at Room Temperature. *Chemosensors* **2024**, *12*, 55. [CrossRef]
6. Zhu, L.; Wang, H.; Qiu, C.; Li, M.; Li, Q.; An, F.; Song, Y.; Wang, T.; Jiao, G.; Ding, Z.; et al. Carbon Monoxide Gas Sensor Based on Hydrothermally Synthesized Pd-CuO Nanorods/$SnSe_2$ Nanoflower Heterojunctions. *ACS Appl. Nano Mater. J.* **2024**, *7*, 25847–25856. [CrossRef]
7. Song, J.; Zhao, J.; Wu, M.; Hu, Y.; Chen, W. Greatly Improved Room-Temperature CO-Sensing Capability of Pt–SnO2 Composite Nanoceramics Prepared Using Solution Reduction Pt-Loading Method. *J. Mater. Sci. Mater. Electron.* **2025**, *36*, 223. [CrossRef]
8. Liu, L.; Zhao, J.; Li, S.; Liu, F.; Jin, Z.; Liu, J.; Du, W.; Wang, F.; Wang, Z.; Wu, L. Room Temperature CO Sensor Based on Au-Decorated ZnO Nanosheets. *Colloids Surf. A Physicochem. Eng. Asp.* **2025**, *717*, 136799. [CrossRef]
9. Wang, W.; Cao, J.; Wang, S.; Zhang, R.; Zhang, Y. CuO–SnO_2 Sensor for Room-Temperature CO Detection: Experiments and DFT Calculations. *Sens. Actuators B Chem.* **2024**, *420*, 136427. [CrossRef]
10. Xie, R.; Lu, J.; Liu, Y. Carbon Monoxide Gas Sensing Properties of SnO2 Modified Metal-Organic Skeleton Derived NiO. *Sens. Actuators A Phys.* **2024**, *367*, 115038. [CrossRef]
11. Zhang, Y.; Xiong, H.; Chen, Q.; Tang, M.; Wang, Z.; Bian, J.; Zhang, D. Hollow-Sphere NiO/Ti_3C_2Tx-Based Gas Sensor for CO Sensing. *ACS Appl. Nano Mater. J.* **2025**, *8*, 4832–4840. [CrossRef]
12. Chen, Y.; Li, X.; Zhu, C.; Fan, G.; Khademolqorani, S.; Banitaba, S.N. Recent Insights on MXene-Based Architectures for Monitoring and Sensing of Gaseous Pollutants: A Review. *Talanta* **2024**, *280*, 126700. [CrossRef] [PubMed]

13. Wang, Y.; Wang, Y.; Jian, M.; Jiang, Q.; Li, X. MXene Key Composites: A New Arena for Gas Sensors. *Nanomicro Lett.* **2024**, *16*, 209. [CrossRef]
14. Berdiyorov, G.R. Effect of Surface Functionalization on the Electronic Transport Properties of Ti_3C_2 MXene. *EPL* **2015**, *111*, 67002. [CrossRef]
15. Zhang, C.J.; Anasori, B.; Seral-Ascaso, A.; Park, S.H.; McEvoy, N.; Shmeliov, A.; Duesberg, G.S.; Coleman, J.N.; Gogotsi, Y.; Nicolosi, V. Transparent, Flexible, and Conductive 2D Titanium Carbide (MXene) Films with High Volumetric Capacitance. *Adv. Mater.* **2017**, *29*, 1702678. [CrossRef]
16. Madbouly, A.; Elzwawy, A.; Morsy, M. Rapid CO Detection Using MWCNTs/SnO_2 Hierarchical Structure: Synthesis, Characterization, and RT Gas Sensing Features. *Ceram. Int.* **2024**, *50*, 25473–25483. [CrossRef]
17. Amith, S.L.; Piraman, S. Effect of Synthesis Technique on the Formation of Surface-Active Reduced Graphene Oxide (RGO) Wrapped SnS_2 Nanosphere Modified Electrode: A Comparative Study on CO Sensing Behaviours. *Surf. Interfaces* **2025**, *72*, 106944. [CrossRef]
18. Shakin, M.S.A.B.; Rahman, M.T.; Shanto, S.N.; Rana, M.M. Au-Loaded WS_2/SnO_2 Heterostructure for Room Temperature Detection of CO at Ppb-Level. *IEEE Sens. J.* **2024**, *24*, 36386–36392. [CrossRef]
19. Yang, Z.; Hu, X.; Wu, M.; Mao, J.; Yang, N.; Wang, X.; Zhang, Q. Mining PANI/Ti_3AlC_2/CeO_2 Ternary Composite CO Sensor: Material Synthesis, Gas Sensing Performance and Mechanism Research. *J. Mol. Struct.* **2025**, *1322*, 140505. [CrossRef]
20. Bai, H.; Guo, H.; Wang, J.; Dong, Y.; Liu, B.; Xie, Z.; Guo, F.; Chen, D.; Zhang, R.; Zheng, Y. A Room-Temperature NO_2 Gas Sensor Based on CuO Nanoflakes Modified with RGO Nanosheets. *Sens. Actuators B Chem.* **2021**, *337*, 129783. [CrossRef]
21. Cao, P.J.; Xu, X.H.; Jia, F.; Zeng, Y.X.; Liu, W.J.; Wang, C.F.; Han, S.; Fang, M.; Liu, X.K.; Zhu, D.L.; et al. Ultrasensitive Room Temperature Chemiresistive NO2 Gas Sensing down to Ppb Levels Using In_2O_3/RGO Heterostructures. *Appl. Surf. Sci.* **2025**, *688*, 162424. [CrossRef]
22. Amu-Darko, J.N.O.; Hussain, S.; Wang, M.; Lei, S.; Alothman, A.A.; Mohammad, S.; Qiao, G.; Liu, G. Advanced 2D Nanosheet-Based Gas Sensor for Sensitive Detection of Low Concentration NO2 Gas Using In_2O_3/Ti_3C_2 Layers. *Sens. Actuators B Chem.* **2024**, *407*, 135464. [CrossRef]
23. Yang, Y.; Zhu, M.; Zhang, H.; Wang, B.; Chen, C.; Li, J.; Wang, Y.; Hao, J. Room Temperature Gas Sensor Based on RGO/Bi_2S_3 Heterostructures for Ultrasensitive and Rapid NO_2 Detection. *Chem. Eng. J.* **2024**, *490*, 151872. [CrossRef]
24. Govind, A.; Bharathi, P.; Harish, S.; Krishna Mohan, M.; Archana, J.; Navaneethan, M. Interface Engineering of a Highly Sensitive Porous CuO Modified RGO Layers for Room Temperature NO_2 Gas Sensor. *Appl. Surf. Sci.* **2024**, *657*, 159604. [CrossRef]
25. Zhang, Y.; Xing, Y.; Yang, Z.; Zhao, L.; Xin, C.; Wei, Z.; Fei, T.; Liu, S.; Zhang, T. Highly Responsive Room-Temperature NO_2 Sensor Based on Oxygen Vacancies-Rich SnO_2-RGO Hybrids. *Mater. Today Commun.* **2024**, *38*, 108090. [CrossRef]
26. Han, J.; Wang, Y.; Zhou, W.; Kong, D.; Gao, Y.; Gao, Y.; Lu, G. Graphene Oxide-Mediated Polymorphic Engineering of In_2O_3 for Boosted NO_2 Gas Sensing Performance. *Sens. Actuators B Chem.* **2025**, *422*, 136613. [CrossRef]
27. Wang, Y.; Fu, J.; Xu, J.; Hu, H.; Ho, D. Atomic Plasma Grafting: Precise Control of Functional Groups on Ti_3C_2Tx MXene for Room Temperature Gas Sensors. *ACS Appl. Mater. Interfaces* **2023**, *15*, 12232–12239. [CrossRef]
28. Guo, F.; Feng, C.; Zhang, Z.; Lili, Z.; Xu, C.; Zhang, C.; Lin, S.; Wu, H.; Zhang, B.; Tabusi, A.; et al. A Room-Temperature NO_2 Sensor Based on Ti_3C_2Tx MXene Modified with Sphere-like CuO. *Senosrs Actuators B Chem.* **2023**, *375*, 132885. [CrossRef]
29. Quan, W.; Shi, J.; Luo, H.; Fan, C.; Lv, W.; Chen, X.; Zeng, M.; Yang, J.; Hu, N.; Su, Y.; et al. Fully Flexible MXene-Based Gas Sensor on Paper for Highly Sensitive Room-Temperature Nitrogen Dioxide Detection. *ACS Sens.* **2023**, *8*, 103–113. [CrossRef]
30. Hilal, M.; Yang, W.; Hwang, Y.; Xie, W. Tailoring MXene Thickness and Functionalization for Enhanced Room-Temperature Trace NO_2 Sensing. *Nanomicro Lett.* **2024**, *16*, 84. [CrossRef]
31. Zhang, Y.; Li, Y.; Jiang, Y.; Duan, Z.; Yuan, Z.; Liu, B.; Huang, Q.; Zhao, Q.; Yang, Y.; Tai, H. Synergistic Effect of Charge Transfer and Interlayer Swelling in V2CTx/SnS2 Driving Ultrafast and Highly Sensitive NO2 Detection at Room Temperature. *Sens. Actuators B Chem.* **2024**, *411*, 135788. [CrossRef]
32. Kodan, S.; Kumar, A.; Sanger, A.; Arora, A.; Malik, V.K.; Chandra, R. Vertically Aligned $MoSe_2$-WS_2 Nanoworms Heterojunction towards Room Temperature NO_2 Gas Sensors. *Sens. Actuators B Chem.* **2024**, *407*, 135481. [CrossRef]
33. Tang, T.; Li, Z.; Cheng, Y.F.; Xie, H.G.; Wang, X.X.; Chen, Y.L.; Cheng, L.; Liang, Y.; Hu, X.Y.; Hung, C.M.; et al. In-Situ Mechanochemically Tailorable 2D Gallium Oxyselenide for Enhanced Optoelectronic NO2 Gas Sensing at Room Temperature. *J. Hazard. Mater.* **2023**, *451*, 131184. [CrossRef]
34. Zhang, X.; Hou, Y.; Wang, J.; Liu, T.; Xu, Z.; Hussain, S.; Qiao, G.; Liu, G. Computational Screening and Experimental Fabrication of $MoSe_2$/3d–TMOS Heterojunction for Room-Temperature Gas Sensor. *Appl. Surf. Sci.* **2024**, *654*, 159465. [CrossRef]
35. Liu, Z.; Lv, H.; Xu, Y.; Shi, K. Sulfur Filling in Oxygen Vacancy and Modulating Surface Active Site on Molybdenum-Based Transition Metal Oxides/Sulfides Heterostructure for Room-Temperature Chemiresistive NO_2 Detection. *Sens. Actuators B Chem.* **2024**, *407*, 135479. [CrossRef]
36. Wang, C.; Chang, X.; Liu, X.; Zhang, J. $ZnIn_2S_4$ Nanosheets for Efficient NO_2 Detection at Room Temperature: Insights into the Role of Sulfur Vacancies. *J. Phys. Chem. Lett.* **2024**, *15*, 5875–5882. [CrossRef] [PubMed]

37. Cheng, X.; Yao, Y.; Zheng, S.; Wan, Y.; Wei, C.; Yang, G.; Yuan, Y.; Tsai, H.S.; Wang, Y.; Hao, J. Te@Se Core-Shell Heterostructures with Tunable Shell Thickness for Ultra-Stable NO_2 Detection. *ACS Sens.* **2025**, *10*, 283–291. [CrossRef]
38. Sun, S.; Li, X.; Wang, N.; Huang, B.; Li, X. A Sensitive Ppb-Level NO_2 Sensor Based on SnO_2 Decorated Te Nanotubes. *Sens. Actuators B Chem.* **2025**, *428*, 137238. [CrossRef]
39. Fan, Y.; Li, L.; Song, B.; Wu, H.; Qi, L.; Khan, M.; Wu, H.; Shi, K. Heterostructures of Hollow Co_3O_4 Nanocages Wrapped in NiO Cilia for Conductometric NO_2 Sensing at Room Temperature. *Sens. Actuators B Chem.* **2024**, *404*, 135299. [CrossRef]
40. Lin, Y.F.; Tseng, Z.C.; Hsueh, W.J.; Chen, J.H.; Huang, C.Y. Room-Temperature Gas Identification via Photochemically Activated p-Type $CuCrO_2$ Nanostructured Films Using Machine Learning. *ACS Appl. Nano Mater.* **2025**, *8*, 189–199. [CrossRef]
41. Wang, B.; Sun, Y.; Dong, Y.; Hou, Y.; Lu, Z.; Wei, Z.; Zhang, W.; Suematsu, K.; Hu, J. Chemiresistive Flexible Gas Sensor for NO_2 Sensing at Room-Temperature Using in Situ Constructed Au@In_2S_3/In_2O_3 Hybrid Microflowers. *Sens. Actuators B Chem.* **2025**, *422*, 136666. [CrossRef]
42. Thathsara, T.; Harrison, C.J.; Hocking, R.K.; Shafiei, M. Pd- and PdO-Decorated TiO_2 Nanospheres: Hydrogen Sensing Properties under Visible Light Conditions at Room Temperature. *Chemosensors* **2023**, *11*, 409. [CrossRef]
43. Yang, J.E.; Kim, S.; Yoon, J.; Lee, J.; Park, I.K.; Kim, K.K. A UV-Photon-Energy-Integrated Gas Sensor Based on Pt-Nanoparticle-Decorated TiO_2 Nanorods for Room-Temperature Hydrogen Detection. *Chemosensors* **2025**, *13*, 177. [CrossRef]
44. Wu, X.; Zhang, Y.; Zhang, M.; Liang, J.; Bao, Y.; Xia, X.; Homewood, K.; Lourenco, M.; Gao, Y. An Ultrasensitive Room-Temperature H_2 Sensor Based on a TiO_2 Rutile–Anatase Homojunction. *Sensors* **2024**, *24*, 978. [CrossRef] [PubMed]
45. Wang, Y.; Chen, C.; Xiao, G.; Chen, C.; He, X.; Zhou, J.; Huang, Z.; Le, J.; Zhou, X. Novel High Performance Room Temperature Hydrogen Sensor—3D In_2O_3@rGO@PPy Aerogel with Dual Enhancement of Mechanical and Gas Sensitive Properties. *Int. J. Hydrogen Energy* **2025**, *154*, 150170. [CrossRef]
46. He, X.; Chen, C.; Liu, Y.; Le, J.; Xiao, G.; Chen, C.; Wang, Y.; Zhou, J. Highly Sensitive Room Temperature Hydrogen Sensor Based on Cactus-like ZnO@3D RGO Aerogel. *Sens. Actuators A Phys.* **2025**, *382*, 116130. [CrossRef]
47. Li, M.; Sun, X.; Wang, Y.; Qin, C.; Cao, J.; Wang, Y. Preparation and Room-Temperature Hydrogen Sensing Property of Flower-like In_2O_3/SnS_2 Nanocomposite. *Phys. E Low-Dimens. Syst. Nanostructures* **2024**, *160*, 115938. [CrossRef]
48. Yang, X.; He, X.; Tang, B.; Zhong, L.; Zhang, W.; Chen, C.; He, T. Room Temperature Hydrogen Sensor of Mace-Like In_2O_3@ZnO Microtubules. *ACS Appl. Electron. Mater.* **2024**, *6*, 5885–5893. [CrossRef]
49. Duan, P.; Wang, H.; Peng, Q.; Chen, S.; Zhou, H.; Duan, Q.; Jin, K.; Sun, J. Ultra-Effective Room Temperature Gas Discrimination Based on Monolithic Pd@MOF-Derived Porous Nanocomposites: An Exclusive Scheme with Photoexcitation. *J. Mater. Chem. A* **2024**, *12*, 3896–3909. [CrossRef]
50. Gautam, D.; Gautam, Y.K.; Kumar, A.; Vikal, S.; Sanger, A.; Malik, A.K.; Pal Singh, B. Highly Selective and Extensive Range Room Temperature Hydrogen Gas Sensor Based on Pd-Mg Alloy Thin Films. *IEEE Sens. J.* **2024**, *24*, 40423–40430. [CrossRef]
51. Kalita, P.; Mondal, B. Humidity Tolerant Enhanced Hydrogen Gas Sensing Using $MoSe_2$-WSe_2 Heterostructures: An Experimental and Computational Insights. *Sens. Actuators B Chem.* **2025**, *424*, 136787. [CrossRef]
52. Li, X.; He, H.; Tan, T.; Zou, Z.; Tian, Z.; Zhou, W.; Bao, Y.; Xia, X.; Gao, Y. Annealing Effect on the Methane Sensing Performance of Pt–SnO_2/ZnO Double Layer Sensor. *Appl. Surf. Sci.* **2023**, *640*, 158428. [CrossRef]
53. Yang, L.; Fu, W.; Mao, L.; Xu, L.; Yao, C.; Zhang, H.; Cheng, H. In_2O_3-ZnO/Laser-Induced Graphene Nanocomposites for a Highly Sensitive, Room-Temperature, Flexible Methane Gas Sensor. *ACS Appl. Nano Mater.* **2025**, *8*, 7510–7519. [CrossRef]
54. Li, X.; Hu, H.; Tan, T.; Sun, M.; Bao, Y.; Huang, Z.; Muhammad, S.; Xia, X.; Gao, Y. Enhancing Methane Gas Sensing through Defect Engineering in Ag-Ru Co-Doped ZnO Nanorods. *ACS Appl. Mater. Interfaces* **2024**, *16*, 26395–26405. [CrossRef]
55. Sun, X.; Zhu, L.; Qin, C.; Cao, J.; Wang, Y. Room-Temperature Methane Sensors Based on ZnO with Different Exposed Facets: A Combined Experimental and First-Principle Study. *Surf. Interfaces* **2023**, *38*, 102823. [CrossRef]
56. Sun, X.; Zhang, Y.; Wang, Y.; Li, M.; Qin, C.; Cao, J.; Wang, Y. UV-Activated AuAg/ZnO Microspheres for High-Performance Methane Sensor at Room Temperature. *Ceram. Int.* **2024**, *50*, 30552–30559. [CrossRef]
57. Li, X.; Tan, T.; Ji, W.; Zhou, W.; Bao, Y.; Xia, X.; Zeng, Z.; Gao, Y. Remarkably Enhanced Methane Sensing Performance at Room Temperature via Constructing a Self-Assembled Mulberry-Like ZnO/SnO_2 Hierarchical Structure. *Energy Environ. Mater.* **2024**, *7*, e12624. [CrossRef]
58. Sun, X.; Zhu, L.; Zhang, Y.; Li, M.; Wang, Y.; Qin, C.; Wang, Y. Simulated Sunlight Enhanced Methane-Sensing Performance Based on Au-Modified ZnO Microsphere under Room Temperature. *J. Mater. Sci. Mater. Electron.* **2023**, *34*, 1950. [CrossRef]
59. Sun, X.; Li, M.; Wang, Y.; Qin, C.; Cao, J.; Wang, Y. NiO/ZnO Heterojunction Microspheres for Methane Detection at Room Temperature. *Opt. Mater.* **2024**, *148*, 114893. [CrossRef]
60. Zabelin, D.; Zabelina, A.; Guselnikova, O.; Miliutina, E.; Kolska, Z.; Stulik, J.; Polansky, R.; Elashnikov, R.; Kalachyova, Y.; Svorcik, V.; et al. Selective Methane Chemiresistive Detection Using MWCNTs Array Decorated by Metal Organic Framework Layer. *Surf. Interfaces* **2023**, *40*, 103105. [CrossRef]

61. Shukla, P.; Saxena, P.; Madhwal, D.; Bhardwaj, N.; Jain, V.K. Electrostatically Functionalized CVD Grown Multiwalled Carbon Nanotube/Palladium Polymer Nanocomposite (MWCNT/Pd) for Methane Detection at Room Temperature. *Chem. Eng. Sci.* **2022**, *264*, 118191. [CrossRef]
62. Hadano, H.; Miyagi, A.; Okuno, T.; Nagawa, Y.; Ishiguro, Y. Development of a Catalytic Combustion Type Gas Sensor with Low Power Consumption. *ECS Trans.* **2016**, *75*, 195–198. [CrossRef]
63. Jang, W.; Kim, I.H.; Jeong, Y.S.; Park, K.B.; Park, S.S.; Yoon, M.Y.; Roh, Y.; Park, J.S. Characteristics of Fabricated Catalytic Combustible Micro Gas Sensor with Low Power Consumption for Detecting Methane Leakage of Compressed Natural Gas Bus. *J. Electroceramics* **2013**, *31*, 280–285. [CrossRef]
64. Yan, W.; Liu, Y.; Bai, Y.; Chen, Y.; Zhou, H.; Ahmad, W. Intelligent MEMS Sensor Based on an Oxidized Medium-Entropy Alloy (FeCoNi) for H_2 and CO Recognition. *ACS Appl. Mater. Interfaces* **2024**, *16*, 49474–49483. [CrossRef]
65. Yang, Y.; Xie, D.; Chen, D.; Geng, L.; Zhang, Y.; Xu, L.; Wu, F. A Quadrilateral Gas Sensor Cell by Complete MEMS Process for Gas Identification. *IEEE Sens. J.* **2024**, *25*, 2267–2275. [CrossRef]
66. Li, M.; Luo, W.; Yan, W. Low Concentration CO Gas Sensor Based on Pulsed-Heating and Wafer-Level Fabricated MEMS Hotplate. *IEEE Electron Device Lett.* **2024**, *45*, 689–692. [CrossRef]
67. Luo, W.; Li, J.; Li, M. A Single MEMS Sensor Based on SnO Nanosheets for Selective Gas Identification. *IEEE Trans. Electron Devices* **2024**, *71*, 7016–7021. [CrossRef]
68. Wu, H.; Yu, J.; Cao, R.; Yang, Y.; Tang, Z. Electrohydrodynamic Inkjet Printing of Pd Loaded SnO_2 Nanofibers on a CMOS Micro Hotplate for Low Power H_2 Detection. *AIP Adv.* **2018**, *8*, 055307. [CrossRef]
69. Li, Z.; Li, M.; Jia, H.; Zhang, H.; Xu, P.; Li, X. High-Sensitive Hydrogen Detection in Oxygen-Free Environment with MEMS Differential Thermopiles. In Proceedings of the IEEE International Conference on Micro Electro Mechanical Systems (MEMS), Austin, TX, USA, 21–25 January 2024; Institute of Electrical and Electronics Engineers Inc.: New York, NY, USA, 2024; pp. 859–862.
70. Yang, Y.; Wei, G.; He, A.; Jiao, S.; Zhang, W.; Gao, C. Design and Optimization of a Novel Multiheater Microhotplate with Thermal Crosstalk. *IEEE Sens. J.* **2025**, *25*, 15893–15905. [CrossRef]
71. Zhang, Z.; Zhao, X.; Wang, D.; Duan, G.; Xing, C. A Micro-Hotplate for MEMS Gas Sensor Wafer Level Packaging. In Proceedings of the 2023 24th International Conference on Electronic Packaging Technology, ICEPT 2023, Shihezi City, China, 8–11 August 2023; Institute of Electrical and Electronics Engineers Inc.: New York, NY, USA, 2023.
72. Wei, G.; Wang, P.; Li, M.; Lin, Z.; Nai, C. Simulation and Optimization of a Planar-Type Micro-Hotplate with Si3N4-SiO2 Transverse Composite Dielectric Layer and Annular Heater. *Micromachines* **2022**, *13*, 601. [CrossRef]
73. Zhang, Z.; Luo, L.; Luo, Y.; Zhang, Z.; Xing, C.; Duan, G. High-Density Integration of Multiple Independent Temperature-Controlled Micro Hotplates for MEMS Gas Sensors. In Proceedings of the Proceedings of IEEE Sensors, Vienna, Austria, 29 October–1 November 2023; Institute of Electrical and Electronics Engineers Inc.: New York, NY, USA, 2023.
74. Li, J.M.; Jiao, M.Z.; Qian, C. Simulation and Performance Study of Low-Power Magnetron Sputtered ZnO Methane Sensor. *Gongcheng Kexue Xuebao/Chin. J. Eng.* **2023**, *45*, 987–994. [CrossRef]
75. Kim, B.J.; Kim, J.S. Gas Sensing Characteristics of MEMS Gas Sensor Arrays in Binary Mixed-Gas System. *Mater. Chem. Phys.* **2013**, *138*, 366–374. [CrossRef]
76. Moon, S.E.; Lee, J.W.; Choi, N.J.; Lee, H.K.; Yang, W.S.; Kim, J.; Park, Y. High-Response and Low-Power-Consumption CO Micro Gas Sensor Based on Nano-Powders and a Micro-Heater. *J. Korean Phys. Soc.* **2012**, *60*, 235–239. [CrossRef]
77. Egger, L.; Sosada-Ludwikowska, F.; Steinhauer, S.; Singh, V.; Grammatikopoulos, P.; Köck, A. SnO_2-Based CMOS-Integrated Gas Sensor Optimized by Mono-, Bi-, and Trimetallic Nanoparticles. *Chemosensors* **2025**, *13*, 59. [CrossRef]
78. Vanmathi, M.; Senthil Kumar, M.; Ismail, M.M.; Senguttuvan, G. Optimization of Process Parameters for Al-Doping Back Ground on CO Gas Sensing Characteristics of Magnetron-Sputtered TiO_2 Sensors. *Mater. Res. Express* **2019**, *6*, 106423. [CrossRef]
79. Hsueh, T.J.; Wu, S.S. Highly Sensitive Co_3O_4 Nanoparticles/MEMS NO_2 Gas Sensor with the Adsorption of the Au Nanoparticles. *Sens. Actuators B Chem.* **2021**, *329*, 129201. [CrossRef]
80. Hsueh, T.J.; Li, P.S.; Fang, S.Y.; Hsu, C.L. A Vertical CuO-NWS/MEMS NO_2 Gas Sensor That Is Produced by Sputtering. *Sens. Actuators B Chem.* **2022**, *355*, 131260. [CrossRef]
81. Kul, O.; Vasiliev, A.; Shaposhnik, A.; Nikitin, A.; Dmitrieva, A.; Bolshakov, A.; Liu, Z.; Ma, M.; Mokrushin, A.; Simonenko, N.; et al. Novel Screen-Printed Ceramic MEMS Microhotplate for MOS Sensors. *Sens. Actuators A Phys.* **2024**, *379*, 115907. [CrossRef]
82. Zhang, D.; Luo, N.; Xue, Z.; Bai, Y.; Xu, J. Hierarchically Porous ZnO Derived from Zeolitic Imidazolate Frameworks for High-Sensitive MEMS NO_2 Sensor. *Talanta* **2024**, *274*, 125995. [CrossRef]
83. Yan, Y.; Lan, X.; Li, Y.; Liang, M.; Liu, X.; Yang, J.; Jia, R.; Ge, Y.; Li, Z.; Huang, L. Oxygen-Vacancy-Rich SnO_2 Nanoparticles Based Ultralow-Power MEMS Sensor for Nitrogen Dioxide Detection. *ACS Appl. Nano Mater.* **2025**, *8*, 6920–6929. [CrossRef]
84. Zhang, M.; He, Z.; Cheng, W.; Li, X.; Zan, X.; Bao, Y.; Gu, H.; Homewood, K.; Gao, Y.; Zhang, S.; et al. A Room-Temperature MEMS Hydrogen Sensor for Lithium Ion Battery Gas Detecting Based on Pt-Modified Nb Doped TiO_2 Nanosheets. *Int. J. Hydrogen Energy* **2024**, *74*, 307–315. [CrossRef]

85. He, Z.; Zhang, M.; Cheng, W.; Li, X.; Zan, X.; Bao, Y.; Gu, H.; Homewood, K.; Gao, Y.; Chang, G.; et al. Reduced Graphene Oxide Modified Nb-Doped TiO_2 Nanosheet for Hydrogen Micro-Electro-Mechanical System Gas Sensor. *Int. J. Hydrogen Energy* **2025**, *100*, 678–687. [CrossRef]
86. Luo, N.; Wang, C.; Zhang, D.; Guo, M.; Wang, X.; Cheng, Z.; Xu, J. Ultralow Detection Limit MEMS Hydrogen Sensor Based on SnO_2 with Oxygen Vacancies. *Sens. Actuators B Chem.* **2022**, *354*, 130982. [CrossRef]
87. Li, Z.; Yu, J.; Dong, D.; Yao, G.; Wei, G.; He, A.; Wu, H.; Zhu, H.; Huang, Z.; Tang, Z. E-Nose Based on a High-Integrated and Low-Power Metal Oxide Gas Sensor Array. *Sens. Actuators B Chem.* **2023**, *380*, 133289. [CrossRef]
88. Sagitova, A.; Markelova, M.; Nikolaeva, A.; Polomoshnov, S.; Generalov, S.; Khmelevskiy, N.; Grigoriev, Y.; Konstantinova, E.; Krivetskiy, V. Restraining SnO_2 Gas Sensor Response Degradation through Heterovalent Doping. *Sens. Actuators B Chem.* **2025**, *429*, 137345. [CrossRef]
89. Niu, F.; Zhou, F.; Wang, Z.; Wei, L.; Hu, J.; Dong, L.; Ma, Y.; Wang, M.; Jia, S.; Chen, X.; et al. Synthesizing Metal Oxide Semiconductors on Doped Si/SiO_2 Flexible Fiber Substrates for Wearable Gas Sensing. *Research* **2023**, *6*, 100. [CrossRef]
90. Li, G.; Wang, X.; Yan, L.; Wang, Y.; Zhang, Z.; Xu, J. PdPt Bimetal-Functionalized SnO_2 Nanosheets: Controllable Synthesis and Its Dual Selectivity for Detection of Carbon Monoxide and Methane. *ACS Appl. Mater. Interfaces* **2019**, *11*, 26116–26126. [CrossRef]
91. Murata, N.; Suzuki, T.; Lin, Y.; Nitani, H.; Niwa, Y.; Wada, T.; Uo, M.; Asakura, K. Structure of Atomically Dispersed Pt in a SnO_2 Thin Film under Reaction Conditions: Origin of Its High Performance in Micro Electromechanical System Gas Sensor Catalysis. *ACS Appl. Mater. Interfaces* **2022**, *14*, 39507–39514. [CrossRef]
92. Gu, F.; Wang, D.; Wang, J.; Wang, P.; Han, D.; Wang, Z.; Qiao, Z.; Hu, Y. Humidity-Independent, Highly Sensitive and Selective NO2Sensor Based on In2O3Nanoflowers Decorated with Graphite Nanoflakes. *IEEE Sens. J.* **2022**, *22*, 14753–14761. [CrossRef]
93. Peveler, W.J.; Binions, R.; Hailes, S.M.V.; Parkin, I.P. Detection of Explosive Markers Using Zeolite Modified Gas Sensors. *J. Mater. Chem. A* **2013**, *1*, 2613–2620. [CrossRef]
94. Yuan, Z.; Sun, H.; Ji, H.; Meng, F. Single Feature to Achieve Gas Recognition: Humidity Interference Suppression Strategy Based on Temperature Modulation and Principal Component Linear Discriminant Analysis. *Sens. Actuators B Chem.* **2025**, *423*, 136842. [CrossRef]
95. Aurora, A. Algorithmic Correction of MOS Gas Sensor for Ambient Temperature and Relative Humidity Fluctuations. *IEEE Sens. J.* **2022**, *22*, 15054–15061. [CrossRef]
96. Wang, Y.; Wang, X.; Zhang, H.; Gao, S.; Xu, W.; Zhao, Y.; Jiao, M.; Huang, S.; Gu, X. Machine-Learning-Aided Identification of Ethanol in Humid Air Using Zinc Complex Capped CsPbBr3 Resistive Sensors. *New J. Chem.* **2023**, *47*, 19077–19086. [CrossRef]
97. Chen, Y.; Hu, J.; Hu, N.; Wu, S.; Lu, Y. Machine Learning-Assisted Pd-Au/MXene Sensor Array for Smart Gas Identification. *Small Struct.* **2025**, *6*, 2400619. [CrossRef]
98. Wang, X.; Zhou, Y.; Zhao, Z.; Feng, X.; Wang, Z.; Jiao, M. Advanced Algorithms for Low Dimensional Metal Oxides-Based Electronic Nose Application: A Review. *Crystals* **2023**, *13*, 615. [CrossRef]
99. Fang, C.; Li, H.-Y.; Li, L.; Su, H.-Y.; Tang, J.; Bai, X.; Liu, H. Smart Electronic Nose Enabled by an All–Feature Olfactory Algorithm. *Adv. Intell. Syst.* **2022**, *4*, 2200074. [CrossRef]
100. Wei, G.; Liu, X.; He, A.; Zhang, W.; Jiao, S.; Wang, B. Design and Implementation of a ResNet-LSTM-Ghost Architecture for Gas Concentration Estimation of Electronic Noses. *IEEE Sens. J.* **2024**, *24*, 26416–26428. [CrossRef]
101. Addae, S.; Kim, J.; Kang, M. Effective Gas Level Prediction Based on Sensor Array Using Deep Learning in Mixed Gases: A Comparative Analysis of CNN-1D, LSTM, and GRU Models. *IEEE Trans. Instrum. Meas.* **2025**, *74*, 1–9. [CrossRef]
102. Wang, T.; Zhang, H.; Wu, Y.; Jiang, W.; Chen, X.; Zeng, M.; Yang, J.; Su, Y.; Hu, N.; Yang, Z. Target Discrimination, Concentration Prediction, and Status Judgment of Electronic Nose System Based on Large-Scale Measurement and Multi-Task Deep Learning. *Sens. Actuators B Chem.* **2022**, *351*, 130915. [CrossRef]
103. Ni, W.; Wang, T.; Wu, Y.; Liu, X.; Li, Z.; Yang, R.; Zhang, K.; Yang, J.; Zeng, M.; Hu, N.; et al. Multi-Task Deep Learning Model for Quantitative Volatile Organic Compounds Analysis by Feature Fusion of Electronic Nose Sensing. *Sens. Actuators B Chem.* **2024**, *417*, 136206. [CrossRef]
104. Mei, H.; Peng, J.; Wang, T.; Zhang, B.; Xuan, F.; Wang, L.; Zeng, M.; Yang, Z. Smart VOCs Recognition System Based on Single Gas Sensor and Multi-Task Deep Learning Model. *Sens. Actuators B Chem.* **2025**, *439*, 137853. [CrossRef]
105. Fu, C.; Zhang, K.; Guan, H.; Deng, S.; Sun, Y.; Ding, Y.; Wang, J.; Liu, J. Progressive Prediction Algorithm by Multi-Interval Data Sampling in Multi-Task Learning for Real-Time Gas Identification. *Sens. Actuators B Chem.* **2024**, *418*, 136271. [CrossRef]
106. Mei, H.; Peng, J.; Wang, T.; Wang, L.; Zhang, B.; Xuan, F. Overcoming Selectivity Challenges in Single Gas Sensor Leveraging Temperature Modulation and Multi-Feature Fusion. *Chem. Eng. J.* **2025**, *522*, 167722. [CrossRef]
107. Zhang, S.; Yuan, Z.; Kong, L.; Wu, Z.; Meng, F. Drift-Like Effect Compensation for the Cyclic Temperature Operation of Semiconductor Gas Sensor. *IEEE Trans. Ind. Electron.* **2025**, *72*, 2140–2149. [CrossRef]
108. Zhang, J.; Jiao, M.; Duan, L.; Zheng, L.; Nguyen, V.D.; Hung, C.M.; Nguyen, D.H. Gas Classification System Based on Hybrid Waveform Modulation Technology on FPGA. *Sens. Actuators B Chem.* **2025**, *435*, 137637. [CrossRef]

109. Zhang, C.; Wang, T.; Zhang, G.; Gao, R.; Gao, C.; Wang, Z.; Xuan, F. Rational Design and Fabrication of MEMS Gas Sensors with Long-Term Stability: A Comprehensive Review. *Adv. Sci.* **2025**, *12*, e11555. [CrossRef] [PubMed]
110. Wang, J.; Yang, P.; Wei, X. High-Performance, Room-Temperature, and No-Humidity-Impact Ammonia Sensor Based on Heterogeneous Nickel Oxide and Zinc Oxide Nanocrystals. *ACS Appl. Mater. Interfaces* **2015**, *7*, 3816–3824. [CrossRef]
111. Zhu, X.; Chang, X.; Tang, S.; Chen, X.; Gao, W.; Niu, S.; Li, J.; Jiang, Y.; Sun, S. Humidity-Tolerant Chemiresistive Gas Sensors Based on Hydrophobic CeO_2/SnO_2 Heterostructure Films. *ACS Appl. Mater. Interfaces* **2022**, *14*, 25680–25692. [CrossRef]
112. Azimi, G.; Dhiman, R.; Kwon, H.M.; Paxson, A.T.; Varanasi, K.K. Hydrophobicity of Rare-Earth Oxide Ceramics. *Nat. Mater.* **2013**, *12*, 315–320. [CrossRef]

Disclaimer/Publisher's Note: The statements, opinions and data contained in all publications are solely those of the individual author(s) and contributor(s) and not of MDPI and/or the editor(s). MDPI and/or the editor(s) disclaim responsibility for any injury to people or property resulting from any ideas, methods, instructions or products referred to in the content.